Spontaneous variations in arousal modulate subsequent visual processing and local field potential dynamics in the ferret during quiet wakefulness

Klaver, L.M.F.; Brinkhof, L.P.; Sikkens, T.; Casado-Román, L.; Williams, A.G.; van Mourik-Donga, L.; Mejías, J.F.; Pennartz, C.M.A.; Bosman, C.A.

DOI
10.1093/cercor/bhad061

Publication date
2023

Document Version
Final published version

Published in
Cerebral Cortex

OXFORD

Cerebral Cortex, 2023, **33**, 7564–7581
https://doi.org/10.1093/cercor/bhad061
Advance access publication date 18 March 2023
Original Article

Spontaneous variations in arousal modulate subsequent visual processing and local field potential dynamics in the ferret during quiet wakefulness

Lianne M.F. Klaver[1], Lotte P. Brinkhof[1], Tom Sikkens[1], Lorena Casado-Román[1], Alex G. Williams[1], Laura van Mourik-Donga[1], Jorge F. Mejías[1,2], Cyriel M.A. Pennartz[1,2], Conrado A. Bosman[1,2,*]

[1]Swammerdam Institute for Life Sciences, University of Amsterdam, Science Park 904, 1098 XH Amsterdam, The Netherlands,
[2]Research Priority Program Brain and Cognition, University of Amsterdam, Amsterdam, The Netherlands

*Corresponding author: Swammerdam Institute for Life Sciences, University of Amsterdam, Science Park 904, 1098 XH Amsterdam, The Netherlands. Email: c.a.bosmanvitttini@uva.nl

Behavioral states affect neuronal responses throughout the cortex and influence visual processing. Quiet wakefulness (QW) is a behavioral state during which subjects are quiescent but awake and connected to the environment. Here, we examined the effects of pre-stimulus arousal variability on post-stimulus neural activity in the primary visual cortex and posterior parietal cortex in awake ferrets, using pupil diameter as an indicator of arousal. We observed that the power of stimuli-induced alpha (8–12 Hz) decreases when the arousal level increases. The peak of alpha power shifts depending on arousal. High arousal increases inter- and intra-areal coherence. Using a simplified model of laminar circuits, we show that this connectivity pattern is compatible with feedback signals targeting infragranular layers in area posterior parietal cortex and supragranular layers in V1. During high arousal, neurons in V1 displayed higher firing rates at their preferred orientations. Broad-spiking cells in V1 are entrained to high-frequency oscillations (>80 Hz), whereas narrow-spiking neurons are phase-locked to low- (12–18 Hz) and high-frequency (>80 Hz) rhythms. These results indicate that the variability and sensitivity of post-stimulus cortical responses and coherence depend on the pre-stimulus behavioral state and account for the neuronal response variability observed during repeated stimulation.

Key words: brain states; in-vivo electrophysiology; oscillations; passive viewing; pupil diameter.

Introduction

When cortical neurons are repeatedly stimulated, their responses are highly variable (Vogels et al. 1989; Arieli et al. 1996). This variability results from the spontaneous activity of anatomically interconnected neurons throughout the cortex and is associated with the animal's behavioral state (Ecker et al. 2010; Harris and Thiele 2011; Schölvinck et al. 2015; Denfield et al. 2018; Jacobs et al. 2020). Behavioral states can exert global influences throughout the cortex and distinctively affect neuronal responses and stimulus perceptibility (Montijn et al. 2015). Therefore, understanding the relationship between behavioral states and cortical activity is critical to elucidate how neuronal variability affects cortical processing.

Behavioral states range from highly active and attentive to deep sleep stages. These states correlate with well-defined electrophysiological patterns of brain activity. For example, high-frequency oscillations and desynchronized waves are predominant during wakefulness, whereas during deep sleep, highly synchronized low-frequency activity patterns dominate brain activity (Steriade et al. 1993; Steriade 2006; Harris and Thiele 2011; McGinley, Vinck, et al. 2015; Sanchez-Vives et al. 2017). During wakefulness, animals can transition between periods of attentive activity and wakeful quiescence. These periods of quiet wakefulness (QW) share features with both active wakefulness (e.g. active behavior, locomotion, increased muscular tone) and sleep (e.g. immobility, hippocampal sharp-wave ripples), and their occurrence depends on internally driven states such as the arousal and attentional level, and externally driven factors such as task requirements and sensory context (Niell and Stryker 2010; Harris and Thiele 2011; Reimer et al. 2014, 2016; Vinck et al. 2015; McGinley, David, et al. 2015; McGinley, Vinck, et al. 2015). In the context of this study, we defined QW as a state in which the animal is awake and receiving passively visual stimulation. Still, the animal is not required to be engaged in a particular task or produce any motor response secondary to the visual stimulation (Crochet and Petersen 2006). In psychophysical tasks, a similar condition would be deemed as "passive attention" (for example, control blocks that contain the same visual stimuli but do not require a response are usually interspersed in visuospatial tasks to account for the stimuli-related activity without attentional load). Although QW has been classically studied as a state that qualitatively differs from active behavior, it has recently been shown to be a dynamic state in which transitions from low-to-high arousal are accompanied by increasing changes in cortical functioning

Received: May 31, 2022. **Revised:** February 11, 2023. **Accepted:** February 14, 2023

(McGinley, David, et al. 2015; Neske et al. 2019). However, it is still unknown how these spontaneous changes in QW affect cortical dynamics during sensory processing. This study aims to elucidate whether spontaneous changes in the arousal state during QW are associated with specific brain signatures and whether these changes might affect visual stimulus processing.

Fluctuations in pupil diameter reflect changes in behavioral state and can occur spontaneously or evoked by stimuli. The locus coeruleus-norepinephrine (LC-NE) system is regularly implicated as the neural substrate of stimulus-evoked pupil dilation via changing arousal state, primarily because of the anatomical connections between the LC and the sympathetic and parasympathetic nervous system (Aston-Jones and Cohen 2005; Joshi et al. 2016; Joshi 2021). Furthermore, brief spontaneous dilations of the pupil diameter during QW correlate with desynchronization of the membrane potential of supragranular cortical neurons and with a decrease of low-frequency power in the neocortex (Reimer et al. 2014, 2016). Thus, continuous fluctuations in behavioral states can be separated according to spontaneous changes in pupil diameter, and groups from both sides of this arousal distribution can be contrasted to unveil differences in cortical dynamics during stimulus processing.

We used the ferret, a research animal model with a visual cortex that has a similar organization as that of primates (Kaschube et al. 2010), to investigate the neuronal correlates of arousal states during QW. We presented full-field and full-contrast gratings to awake, head-fixed ferrets and studied rhythmic changes in the local field potential (LFP) and spiking activity of neurons in ferret primary visual cortex (area 17, V1) and the posterior parietal cortex (PPc), a higher order sensory area that shows connections to visual cortical areas (Dell et al. 2019). We found that pre-stimulus pupil diameter spontaneously fluctuated during QW. We separated the distribution of pupil diameters into quintiles and compared the electrophysiological changes observed in the lowest and highest quintiles of the distribution. During short periods of pre-stimulus pupil dilation, corresponding to periods of high arousal during QW, we observed an increase in orientation tuning selectivity and spike-count correlations between spiking responses.

Furthermore, we observed amplitude and peak shifts of the spectral power of the LFP signal depending on the QW arousal state. Despite the decrease in power, the high-arousal quintile within QW states triggered low-frequency interareal increments in coherence, and computational models able to reproduce these effects pointed towards feedback (FB) signals from higher brain areas as a potential cause. The high-arousal condition in QW also led to frequency-dependent phase-locking of different neuronal types in the striate cortex. Our results show that the variability and sensitivity of cortical responses to a stimulus critically depend on the animal's behavioral state before stimulus onset.

Materials and methods

All animal experiments were conducted with the approval of the local ethical committee of the University of Amsterdam and the Netherlands National Committee for the protection of animals used for scientific purposes. We used 6 healthy, adult female ferrets (*Mustela putorius furo*) of approximately 6 months old at the onset of the study. Ferrets were group-housed, maintained under a 16/8 h dark/light cycle, and received water and food ad libitum.

Stimulation paradigm. We used custom software coded in MATLAB (*Mathworks*) and the Psychophysics Toolbox (Brainard 1997) to present visual stimuli to awake ferrets. All stimuli were presented on an LCD monitor (53.3 x 33 cm, refresh rate 60 Hz). During the electrophysiological recordings, the ferrets were positioned on an elevated platform inside a sound-attenuated Faraday cage and habituated to sitting comfortably in a custom-made cylindrical body holder (Fig. 1A). We placed the monitor at ∼25 cm in front of the animals (Fig. 1A). Visual stimuli consisted of presenting a whole field chevron pattern (SF = 0.18 cycles/deg, TF = 1.2°/s) for 1 s in 8 different orientations (0°–315° in steps of 45°), interspersed with an intertrial interval (ITI) segment of an isoluminant gray screen, shown for 0.35 s with a random jitter of ±20 ms (Fig. 1B). Following 11 stimulus repetitions, we presented another isoluminant gray screen for 3 s to record baseline activity. We tracked eye position and pupil diameter based on the corneal reflection of light with a noninvasive monocular eye tracker (ISCAN ETL-200, Rodent Eye Tracking Lab).

Headpost implantation. To maintain a stable visual field throughout recordings, ferrets received a cranial headpost-implant in two separate surgeries. First, ferrets were implanted with a titanium baseplate under aseptic and sterile surgical conditions. The baseplate was screwed to the skull's frontal bone with four titanium screws and fortified using C&B Super Bond (Parkell) under general anesthesia. We used Ketamine (10 mg/kg) and Dexdomitor (0.08 mg/kg) administered i.m. to induce general anesthesia, and isoflurane (1–3%) delivered in 100% medical-grade O_2 for maintenance. Marcaine 0.5% was used as a local anesthetic for intubation. Also, we used Buprenorphine (0.01 mg/kg, s.c., preoperative) and Meloxicam (0.2 mg/kg, s.c., peri- and post-operative) as analgesia; and Amoxicillin (20 mg/kg, s.c., in a single-dose peri- and post-operative) for antibiotic prophylaxis. Atropine (0.05 mg/kg, s.c.) and Dopram (5 mg/kg, s.c.) were used in case of respiratory distress. Dehydration was prevented using 50 mL of saline (0.9%, s.c.). We routinely monitored the respiratory rate, heart rate, and internal body temperature during surgery to maintain physiological values (LifeVet M, Eickemeyer). We used Antisedan (0.8 mg/kg, i.m.) to reverse the action of Dexdomitor at the end of the surgery. After an average of four weeks of ossification around the baseplate's anchor screws, we installed a head-post pole under light isoflurane anesthesia to allow head-fixed electrophysiological recordings. A small skin incision was performed above the baseplate, and the pole was attached and secured with Loctite 242. Meloxicam (0.2 mg/kg, s.c.) was used as post-operative analgesia.

Electrode implantation. Under the same surgical conditions, we performed a 1.5 mm diameter craniotomy over the primary visual cortex of the ferret (area 17, V1) using cranial, gyral, and sulcal landmarks (Innocenti et al. 2002; Manger et al. 2004). Once the dura was exposed and retracted, a 32-channel multielectrode silicon probe (Models A4 x 8–5 mm-200-400-177-CM32 and A2 x 16–10 mm-100-500-177-CM32, NeuroNexus) was inserted approximately 1.5 mm along the dorsoventral axis in the visual cortex ($n = 6$). In addition, half of these animals ($n = 3$) received an additional implant of the same probe in area PPc. The electrophysiological implant was covered with a protective cap and chronically fixed with dental cement (Simplex Rapid Acrylic Powder, Kemdent). Then, the wound was closed by suturing the skin or gluing with Vetbond (3 M). Finally, the electrode placement was verified post hoc using a conventional Nissl staining procedure in brain slices of 100 μm thickness.

Electrophysiological recording techniques and signal preprocessing. We recorded spiking, and LFP activity in V1 and PPc using an analog Neuralynx ERP-54 system and collected data with the CheetahRev 5.6.3 (Hardware SubSystem Cheetah 64) software. The signals were recorded with an input range of 1,506 μV and

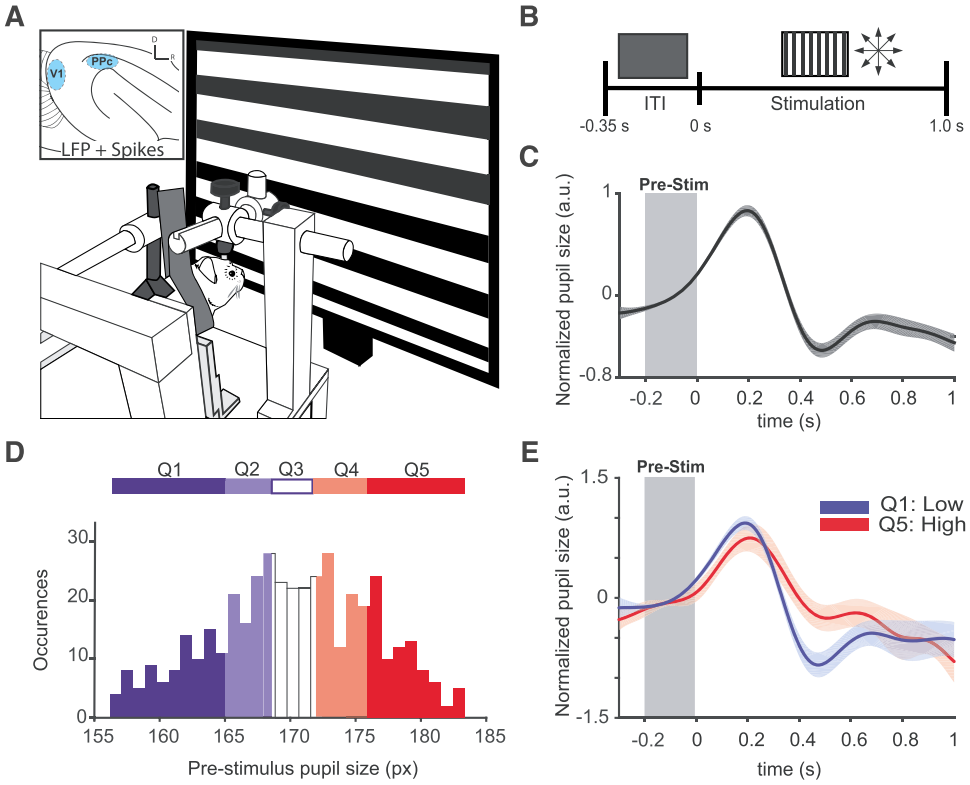

Fig. 1. Spontaneous pupil fluctuations during passive visual stimulation. (A) Experimental design. Awake head-fixed ferrets were placed in a cylindrical holder, to which they were familiarized, in front of a computer screen displaying visual stimuli. Inset: a schematic of the ferret cortex displaying the target areas for recordings (V1 and PPc). (B) The experiment consisted of the presentation for 1 s of a drifting grating (SF = 0.18 cycles/deg, TF = 1.2°/s) for 8 different orientations. During the ITI, a gray screen was presented for 0.35 s with a SOA of ±0.02 s. (C) Pupil response of one ferret normalized over all trials. For visualization purposes, pupil trials were smoothed with a low-pass Butterworth filter with a cut-off frequency of 3 Hz and subsequently averaged across all ferrets and sessions. The onset of the stimulus occurs at 0 s. The period of 0.2 s before stimulus onset (in gray) corresponds to the pre-stimulus control window. (D) Pre-stimulus pupil sizes (expressed as number of pixels, *px*) were divided into quintiles. (E) Pupil responses for the first quintile (Q1, low arousal) and the last quintile (Q5, high arousal) normalized per quintile. The normalized data show a similar pupil dynamic range for both conditions (Joshi 2021).

a sampling frequency of 30,303 Hz in 32 continuously sampled channels (CSC). The electrophysiological signals were amplified with an amplitude gain of 830 dB and filtered with a band-pass filter between 0.1 and 9,000 Hz. Transistor–transistor logic pulses for time stamping of stimulus presentation were serially sent through an Arduino Board Mega 2560 to the acquisition system. All signals were recorded continuously for the entire duration of the recording session. The recorded signals were processed offline using the FieldTrip toolbox (https://www.fieldtriptoolbox.org/) for electrophysiological analyses (Oostenveld et al. 2011) and MATLAB custom software. We used the open-source software Kilosort2 to extract single-unit spikes from the broadband signal (Pachitariu et al. 2016). Following automatic spike detection, we performed an additional manual curation of those spikes ambiguously separated. The multi-unit activity was obtained from the broadband signal using a high-pass filter at 500 Hz (Butterworth filter, second order). For LFP analyses, the original broadband signal was detrended, linearly downsampled to 1,024 Hz, and low-pass filtered with a Butterworth filter (second order) with a cut-off frequency of 100 Hz. We removed powerline artifacts from the LFP using a band-stop filter centered at 50 Hz and harmonics. Then, we segmented the continuous signals in epochs of interest, for each channel, between 0.3 s pre-stimulus onset and 1 s post-stimulus onset.

Trial inclusion criteria and grouping. We visually inspected the stimulus-evoked-pupil response of the eye-tracking recordings to assess the quality of the traces. We eliminated those trials in which motor artifacts were identified and when an accurate pupil size could not be determined during the presentation of visual stimuli or the pre-stimulus baseline. To determine the arousal state of the animal before stimulation and define the high- and low-arousal conditions, we selected a time epoch between −0.2 s and stimulus onset as a pre-stimulus baseline window. From this window, we obtained the distribution of the average pupil size. We then divided the pre-stimulus pupil size distribution into quintiles (Figs. 1D and Fig. 3A), selecting the trials of the 1st and 5th quintiles for further analysis. We denominated those trials of the 1st quintile as the low-arousal group (condition QW-low arousal) and the 5th quintile as the high-arousal group (condition QW-high arousal).

Orientation selectivity index. We calculated an orientation selectivity index (OSI) to measure the orientation-tuning properties of the recorded neurons in the ferret primary visual cortex. First, we computed the mean discharge rate (in spikes/s) for each stimulus orientation (8 in total) using a spike density function and convolving the spike trains with a gaussian kernel. Then, after identifying the orientation that evoked the highest rate over trials ($Rate_{pref}$) and inferring the orthogonal orientation ($Rate_{non\text{-}pref}$), we computed the neuronal *d'* (Berens et al. 2008; Meijer et al. 2017, 2020) as an OSI, a measure that includes the pooled variance across neurons, according to the formula:

$$OSI = \frac{Rate_{pref} - Rate_{nonpref}}{\sqrt{\frac{\sigma_{pref} + \sigma_{nonpref}}{2}}} \quad (1)$$

Following Meijer et al. (2017), we selected an OSI > 0.4 as a cut-off value to classify a neuron as orientation-selective.

Spike-count correlations (r_{SC}). To obtain the pre- and post-stimulus correlated variability of spiking responses across high- and low-arousal conditions, we calculated the Pearson's correlation of spike counts (noise correlations) for every pair of simultaneously recorded single units (Cohen and Kohn 2011) from the ferret primary visual cortex. To remove the potential influence of confounding variables that could affect the variability of spiking responses, we transformed all spike counts from every neuron into a z-score using the mean and SD for every repetition of both experimental conditions (Nandy et al. 2017; Arbab et al. 2018). Then, we pooled these z-scored values in pairs of neurons and obtained the Pearson's correlation from these pairs. The r_{SC} was calculated for each condition using a spike-counting window of 0.2 s across the entire epoch of interest Fig. 2B. We controlled the trial-to-trial variability in spike-count correlations by shuffling the neurons across conditions before calculating the r_{SC} and repeating the analysis through different spike-count windows, ranging from 0.05 to 0.3 s (Kass and Ventura 2006; Arbab et al. 2018).

Spectral analysis of power. The raw LFP data from each channel were separated into 2 groups (QW-high and QW-low arousal conditions) corresponding to the 1st and 5th quintiles of the pupil size distribution across trials. The resulting epochs of interest were demeaned and divided by their standard deviation. From these segments, we used a 1 s segment of the baseline window (from 1.5 to 2.5 s) and a 1 s period from the stimulus onset, comprising the entire visual stimulation. Then, we obtained the spectrally decomposed Fourier coefficients of every epoch of interest (per channel), applying a discrete fast Fourier transform (FFT) to the segmented trials.

We used the irregular-resampling auto-spectral analysis (IRASA) method to obtain the spectral power, which isolates the oscillatory components from the fractal (1/*f*) activity of the power spectrum of any neurophysiological signal (Wen and Liu 2015). IRASA estimates the oscillatory and fractal power spectral components by resampling the neural signal using multiple non-integer positive numbers and their reciprocals. Then, it calculates the geometric mean of the auto-power spectra of each resampled signal. The resulting spectrum contains a redistribution of the fundamental and the harmonic oscillatory frequencies by an offset that varies with the resampling factor. Conversely, the fractal component of the spectral estimation remains constant independently of the resampling factor. Finally, we obtained an approximate estimate of the power spectrum of the oscillatory component by subtracting the median of the mean auto-power spectra (containing the fractal estimation of the power) from the original power spectrum (obtained from the previously calculated Hanning tapered Fourier coefficients). The power estimates were normalized per session and animal relative to the mean power between 4 and 100 Hz (Malkki et al. 2016).

Phase-locking of LFP–LFP signals. The LFP–LFP phase-locking value across electrodes was calculated using the weighted phase lag index (WPLI), a bivariate metric of the phase consistency across signals, less affected by volume conduction, noise, and sample size (Vinck et al. 2011). Specifically, the WPLI estimates, for a particular frequency, the non-equal probability of phase leads and lags of the imaginary part of the cross-spectrum, weighted by the magnitude of this imaginary part of the cross-spectrum. The WPLI was computed using the equation:

$$\Phi = \frac{\left|\mathbf{E}\left\{\Im\left\{\mathbf{X}\right\}\right\}\mathbf{sgn}\left(\Im\left\{\mathbf{X}\right\}\right)\right|}{\mathbf{E}\left|\Im\left\{\mathbf{X}\right\}\right|} \quad (2)$$

where the expression $\mathbf{E}\{\Im\{\mathbf{X}\}\}$ represents the estimation of the imaginary part of the cross-spectrum between 2 channels, and the expression $\mathbf{sgn}()$ the signed function of that estimator. The WPLI metric was estimated from a 4-tapered multitaper Fourier decomposition (Jarvis and Mitra 2001) over an epoch of 1 s duration, resulting in a spectral smoothing of ±2 Hz.

Phase locking of spike-LFP signals. The strength of the phase-locking between the LFP and the spikes was measured using the pairwise phase consistency (PPC) analysis (Vinck et al. 2012). For each frequency bin *f*, we determined spike-LFP phases in epochs of 5/*f* (5 cycles) length centered around the spikes obtained during the baseline and stimulation period. The PPC index was obtained from the Kaiser-tapered ($\beta = 3$) Fourier coefficients and calculated according to the formula:

$$\psi = \frac{\sum_{m=1}^{M}\sum_{l\neq m}^{M}\sum_{j=1}^{N_m}\sum_{k=1}^{N_m}\left(\sin\left(\theta_{j,m}\right)\sin\left(\theta_{k,l}\right)+\cos\left(\theta_{j,m}\right)\cos\left(\theta_{k,l}\right)\right)}{\sum_{m=1}^{M}\sum_{l\neq m}^{M}N_m N_l} \quad (3)$$

where $\theta_{j,m,}$ and $\theta_{k,l}$ are the *j*th and *k*th spikes at frequency *f* in trial *m* and trial *l*, respectively. N_m and N_l denote the number of spikes *N* in different trials. This method solves the problem of statistical dependence between spike-LFP phases because it restricts the PPC analysis to those spikes recorded from separate trials (Vinck et al. 2012). The PPC analysis was calculated using the *spiketriggeredspectrum* function (method: ppc1) from the FieldTrip toolbox (Oostenveld et al. 2011). The PPC index was calculated per each neuron individually. The resultant PPC spectra were averaged across all neurons.

Computational model. The computational model is based on our previous work (Mejias et al. 2016; Lindeman et al. 2021) and involves 3 levels of description: intra-laminar, inter-laminar, and inter-areal (Fig. 5A). We consider 2 cortical regions at the inter-areal level: the primary visual cortex (area 17, V1) and the PPc. Each area consists of 2 cortical layers, or laminar modules, which represent the inter-laminar level and simulate the dynamics of superficial (2/3) and deep (5/6) layers, respectively. Each laminar module has 1 excitatory and 1 inhibitory population (e.g. intra-laminar level) modeled using firing rate dynamics. Their respective firing rates $r_E(t)$ and $r_I(t)$ are described by the following equations:

$$\tau_E \frac{dr_E(t)}{dt} = -r_E(t) + F(I_E)\sqrt{\tau_E}\,\xi_E(t) \quad (4)$$

$$\tau_I \frac{dr_I(t)}{dt} = -r_I(t) + F(I_I) + \sqrt{\tau_I}\,\xi_I(t) \quad (5)$$

Here, τ_E and τ_I are the time constants for the excitatory and inhibitory populations, respectively. $\xi_E(t)$ and $\xi_I(t)$ are the Gaussian white noise terms of zero mean and standard deviation (σ) one. For superficial layers, we chose $\tau_E = 6$ **ms**, $\tau_I = 15$ **ms** for the time constants and $\sigma = 0.3$ for the noise strength, which leads to a noisy oscillatory dynamic in the gamma range. For deep layers, we chose $\tau_E = 42$ ms, $\tau_I = 105$ ms and $\sigma = 0.45$, which leads to a noisy oscillator in the alpha-band frequency range. The relatively large values for the time constants in deep layers are thought to reflect other slow biophysical factors not explicitly included in the model, such as the dynamics of NMDA receptors.

The function $F(x) = x/(1 - \exp(-x))$ is the input–output transfer function, applied for simplicity to all excitatory and inhibitory neuronal populations, which transforms the incoming input currents into their corresponding cell-averaged firing rates. The argument of the transfer function is the incoming current for each population, which involves (i) a background term, (ii) a local term,

Table 1. Parameter values of the computational model for V1–PPc laminar interactions.

Parameter	Value (layer)	Parameter	Value (state)
τ_E	6 ms (sup), 42 ms (deep)	w_{EE}	1.5
τ_I	15 ms (sup), 105 ms (deep)	w_{IE}	3.5
σ	0.3 (sup), 0.45 (deep)	w_{EI}	3.25
I_{bg}	3 (sup), 2 (deep)	w_{II}	2.5
w_{ds}	1	$J_{A\text{-}d}$	1 (10 for high arousal)
w_{sd}	0.75	$J_{A\text{-}s}$	0.3 (3 for high arousal)
J_{FF}	0.5	$J_{FB\text{-}I}$	0.5
$J_{FB\text{-}s}$	1.6	$J_{FB\text{-}d}$	0.2

and (iii) a long-range term. The incoming current for excitatory and inhibitory populations, respectively, is:

$$I_E = I^E_{bg} + I^E_{\text{local}} + I^E_{lr} \tag{6}$$

$$I_I = I^I_{\text{local}} + I^I_{lr} \tag{7}$$

The background term is a default constant current only received by excitatory neurons in V1 and area PPc. It equals $I^E_{bg} = 3$ for superficial excitatory neurons and $I^E_{bg} = 2$ for deep excitatory neurons. This term already includes the effects of the passive visual input received by V1 during the experiment. The local term involves the input coming from neurons within the area, and is given by:

$$I^E_{\text{local}} = w_{EE} r_E - w_{EI} r_I + I^E_{\text{interlaminar}} \tag{8}$$

$$I^I_{\text{local}} = w_{IE} r_E - w_{II} r_I + I^I_{\text{interlaminar}} \tag{9}$$

Here, w_{ab} are the synaptic weights from population b to a (see Table 1 for numerical values). The interlaminar terms represent contributions from a different layer than those terms used for the population under scrutiny. The only interlaminar projections are from superficial excitatory to deep excitatory neurons, with synaptic strength $w_{ds} = 1$, and from deep excitatory to superficial inhibitory neurons, with strength $w_{sd} = 0.75$ (Mejias et al. 2016).

With these parameters compatible with experimental values, the model produces noise-driven oscillators through stochastically perturbed stable focus dynamics—i.e. the activity behaves like a physical damped oscillator, which is kicked out of the fixed point by existing fluctuations. Furthermore, contrary to other models (Wilson and Cowan 1972), which often utilize a limit cycle dynamic, the oscillatory activity produced here is weakly coherent from one cycle to another, providing a closer match to the highly irregular rhythmic activity of LFPs in actual neuronal recordings and reproducing a wide range of experimental findings (Mejias et al. 2016; Lindeman et al. 2021). Finally, the long-range term (I^E_{lr} and I^I_{lr} Eqs 6 and 7) in the input current includes currents coming from other neocortical areas. These currents follow the general form $J_{ab} r_b$, (with J_{ab} being the synaptic strength from area b to area a). Therefore, we will specify only the synaptic coupling strengths to characterize them.

Following anatomical evidence widely consistent for mammals (Markov et al. 2014; Harris et al. 2019), we consider feedforward (FF) projections from primary visual to posterior parietal cortices originating in layer 2/3 pyramidal V1 neurons and target (indirectly via layer 4, which is not explicitly included in the model) pyramidal neurons in PPc layer 2/3 (with a synaptic strength of $J_{FF} = 0.5$). Feedback (FB) projections stem from pyramidal neurons in deep layers of PPc and target pyramidal neurons in superficial (strength of $J_{FB\text{-}s} = 1.6$) and deep layers (strength of $J_{FB\text{-}d} = 0.2$), and inhibitory neurons in superficial and deep layers (strength of $J_{FB\text{-}I} = 0.5$ for both cases). The long-range terms for the excitatory and inhibitory populations for each area and layer (indicated by super or subindices) are therefore described by the following equations:

$$I^{V1,L2/3E}_{lr} = J_{FB-s}\, r_{PPC,L5/6E} \tag{10}$$

$$I^{V1,L2/3I}_{lr} = J_{FB-I} r_{PPC,L5/6E} \tag{11}$$

$$I^{V1,L5/6E}_{lr} = J_{FB-d} r_{PPC,L5/6E} \tag{12}$$

$$I^{V1,L5/6I}_{lr} = J_{FB-I} r_{PPC,L5/6E} \tag{13}$$

$$I^{PPC,L2/3E}_{lr} = J_{FF} r_{V1,L2/3E} \tag{14}$$

$$I^{PPC,L2/3I}_{lr} = I^{PPC,L5/6E}_{lr} = I^{PPC,L5/6I}_{lr} = 0 \tag{15}$$

Arousal signals to these cortical areas are modeled as top–down FB inputs arriving mostly in deep PPc layers (with a strength of $J_{A\text{-}d} = 1$ for the low arousal case) and in superficial layers of V1 (strength of $J_{A\text{-}s} = 0.3$ for low arousal, see Table 1), in agreement with recent hypotheses about the dependence of FB targets on the hierarchical distance of the projections (Markov et al. 2014). For the high-arousal signal, these top–down arousal inputs are multiplied by 10.

To mimic the depth of the recording electrodes for V1 and PPc in experiments, we estimate the LFP signal in the model by a weighted average of the excitatory superficial and deep layers, with a superficial-to-deep ratio of 2:8 for both areas (i.e. 20% and 80% weight of the superficial and deep layers, respectively). These simulated signals were then used to compute spectral coherence (as in Mejias et al. 2016) and the WPLI index.

Statistical testing. We assessed significant differences between conditions using a nonparametric statistical approach (Wilcoxon rank-sum and sign tests) with a significance threshold of $P < 0.05$. For the connectivity analyses, we calculated a nonparametric permutation test of the coherence differences (Maris et al. 2007), adjusted by a multiple comparison correction at the subject level (Scheeringa et al. 2011). First, the individual differences between electrodes (within-subjects) were computed using a Welch t-statistic. Next, we obtained individual P-values of the t-Welch differences from a Student's t cumulative distribution function, using the Welch-Statterth-Waite equation to estimate the degrees of freedom of every distribution, and a cluster-based approach across frequencies to select significant frequency band clusters (Maris and Oostenveld 2007). Then, we built a null distribution of these frequency bin clusters by computing a paired sample t-test and randomly exchanging the condition labels between conditions. We repeated this step across 1,000 permutations of the data retaining the maximum and minimum values of the cluster-selected values. Finally, we compared the observed T-statistics to the maximal and minimum distributions. T-statistics were considered significant at $P < 0.05$ if they were below the 2.5th percentile of the minimum or above the 97.5th percentile of the maximal distribution. We used a generalized linear mixed model (GLMM) to evaluate the power changes due to arousal considering the variability across animals and channels as random effects (Tuerlinckx et al. 2006; Johnson et al. 2015). The statistical significance of the GLMM was tested using a likelihood

ratio test under a χ^2 distribution with a significant threshold set at $P < 0.05$.

Results

To investigate the effects of spontaneous arousal changes during QW on cortical microcircuits, we recorded the LFP signal and spiking activity from the ferret primary visual cortex (area 17) and the caudal part of the posterior parietal cortex (PPc) from sixferrets. Ferrets passively viewed full-screen gratings at eight different orientations for 1 s while we continuously recorded pupil diameter changes. These pupil diameter changes were used to infer the behavioral state of the animal (Fig. 1A and B, Supplementary Fig. 1).

Pupil diameter spontaneously fluctuates during quiet wakefulness

We first focused on the pupil response of the animal during stimulus presentation (Supplementary Fig. 1A shows an example of a 30 s pupil recording). Fig. 1C shows an example of a normalized pupil trace. Supplementary Fig. 1B shows the non-normalized version of those pupil traces). As expected, pupil illumination produces a typical event-related response consisting of pupil dilation followed by a constriction that undershoots the pre-stimulus size period (Wang and Munoz 2015; Wang et al. 2017). We wondered whether this event-related pupil fluctuation could be affected by the behavioral state of the ferret. Therefore, we calculated the area of the pupil (in pixels) in a pre-stimulus window between 0.2 and 0 s pre-stimulus onset (Fig. 1C, Supplementary Fig. 1), using the average of that window as an indicator of the animal's behavioral state before the stimulus appeared (Aston-Jones and Cohen 2005; Joshi et al. 2016; Joshi and Gold 2020; Joshi 2021).

We used the average of this pre-stimulus window to create a pupil size distribution that we separated into quintiles (Fig. 1D). Based on the distribution of pupil sizes, we considered those trials from the first quintile (Q1) exhibiting maximum constriction as low-arousal trials. Conversely, the last quintile (Q5) trials displaying maximum dilation were considered high-arousal trials. Since both quintiles pertain to a distribution of a QW state, we denominate both conditions as QW-low (QW-L) and QW-high (QW-H) arousal, respectively. We used ~80 trials per session per condition for subsequent analyses.

The normalized event-related pupil response shows a similar dynamic for QW-L and QW-H arousal trials (Fig. 1E. Supplementary Fig. 1C). In both conditions, the event-related pupil response consists of a post-stimulus dilation followed by pupil constriction. This constriction predominates during QW-L. Still, the similar shape of the response suggests that the pupil diameter spontaneously increases during passive stimuli, similarly for low- and high-arousal conditions.

High arousal increases the selectivity of spiking responses during quiet wakefulness

Active behavioral states improve neuronal coding efficiency in area V1 of primates (Shadlen and Newsome 1998; Mitchell et al. 2007; Cohen and Maunsell 2009; Ecker et al. 2010; Nandy et al. 2017; Denfield et al. 2018) and mice (Niell and Stryker 2010; Keller et al. 2012; Reimer et al. 2014, 2016; Vinck et al. 2015; Leinweber et al. 2017), but it is unknown whether encoding improvement can be observed during quiescence. Therefore, we investigated whether high- and low-arousal QW states contribute differently to the coding efficiency of cortical neurons. To answer this question, we recorded 145 single units from the primary visual cortex while ferrets passively observed 8 different orientations of full-contrast gratings for 1 s per trial. From these 145, 110 neurons (75.8% of the total) responded to the presentation of visual stimuli (see Supplementary Fig. 2A and B for a peri-stimulus time histogram example for each condition). We checked whether different QW states change the spike rate of neurons responding to the stimulus presentation by computing an average spike rate across the stimulus presentation window. Previous studies have shown a decrease in the spiking rate of high-arousal quiescent periods following active locomotion, but the spiking rate within quiescent periods remains unaffected (McGinley, Vinck, et al. 2015). In agreement with these results, we observed that the spike rate of striate cortex neurons in different QW states does not change with passive stimulation (Supplementary Figs. 2A and B, Fig. 2A, QW-L: 7.9 ± 0.7 Hz, QW-H: 8.2 ± 0.7 Hz, $P = 0.86$, Wilcoxon rank-sum test: rank-sum = 2.1 x 10^4).

We next focused on the correlated variability across neurons. An increase of correlated variability in a neuronal population is usually associated with decreased quality of the information represented in a population response (Shadlen and Newsome 1998; Averbeck and Lee 2006; Mitchell et al. 2009; Cohen and Kohn 2011; Arbab et al. 2018) (but see Montijn et al. 2016) and can be modulated by active locomotion and attentional state (Reynolds et al. 2000; Cohen and Maunsell 2009; Mitchell et al. 2009; Reimer et al. 2014; Vinck et al. 2015). Therefore, we evaluated the response variability between the pairs of neurons during QW states using spike-count correlations (r_{SC}) between primary visual cortex neurons with an integration window of 0.2 s (Fig. 2B). These correlations reflect the functional state of neuronal networks across time (Cohen and Kohn 2011). After stimulus onset, both conditions showed r_{SC} values above the chance level, indicating significant correlations. In addition, QW-H showed a transient increase of r_{SC} approximately at 0.1 s after stimulus onset ($P < 0.05$, nonparametric randomization test across neurons). Under both conditions, the r_{SC} slowly rose across time after 0.1 s post-stimulus onset, decreasing to baseline levels after stimulus offset. Finally, we controlled for bin size effects by calculating the r_{SC} centered at 0.1 s post-stimulus onset with integration windows of different sizes (Fig. 2C). In all these cases, QW-H showed higher significant spike-count correlations than QW-L ($P < 0.05$, nonparametric randomization test across neurons), indicating that state fluctuations within QW can lead to different intra-areal spike correlations. Notably, our results show that the stimulus onset during quiescent states can trigger an increase of r_{SC} despite high arousal, suggesting, contrary to earlier findings (Shadlen and Newsome 1998; Averbeck and Lee 2003; Mitchell et al. 2009; Arbab et al. 2018), that a rise in spike-count correlations might contribute to improving the information processing efficiency during periods of increased arousal.

Previous studies have shown that active states effectively increase the orientation selectivity of striate neurons (Niell and Stryker 2010; Reimer et al. 2014; Vinck et al. 2015). For this reason, we evaluated whether QW-L and QW-H modulate the selectivity of the response of visual cortex neurons to drifting gratings using an OSI, which considers the pooled response variability from different neurons across preferred and non-preferred orientations (see Section Methods). We observed that the spike rate on neurons at their preferred orientation was modestly but significantly higher during QW-H (Fig. 2D, $P < 0.05$, nonparametric randomization test across neurons). Furthermore, OSI values significantly increased at the population level during pupil dilation (Fig. 2E, $P = 0.023$, sign test: sign differences = 48, $z = 2.26$). From 142 recorded neurons, 53% showed an increment of

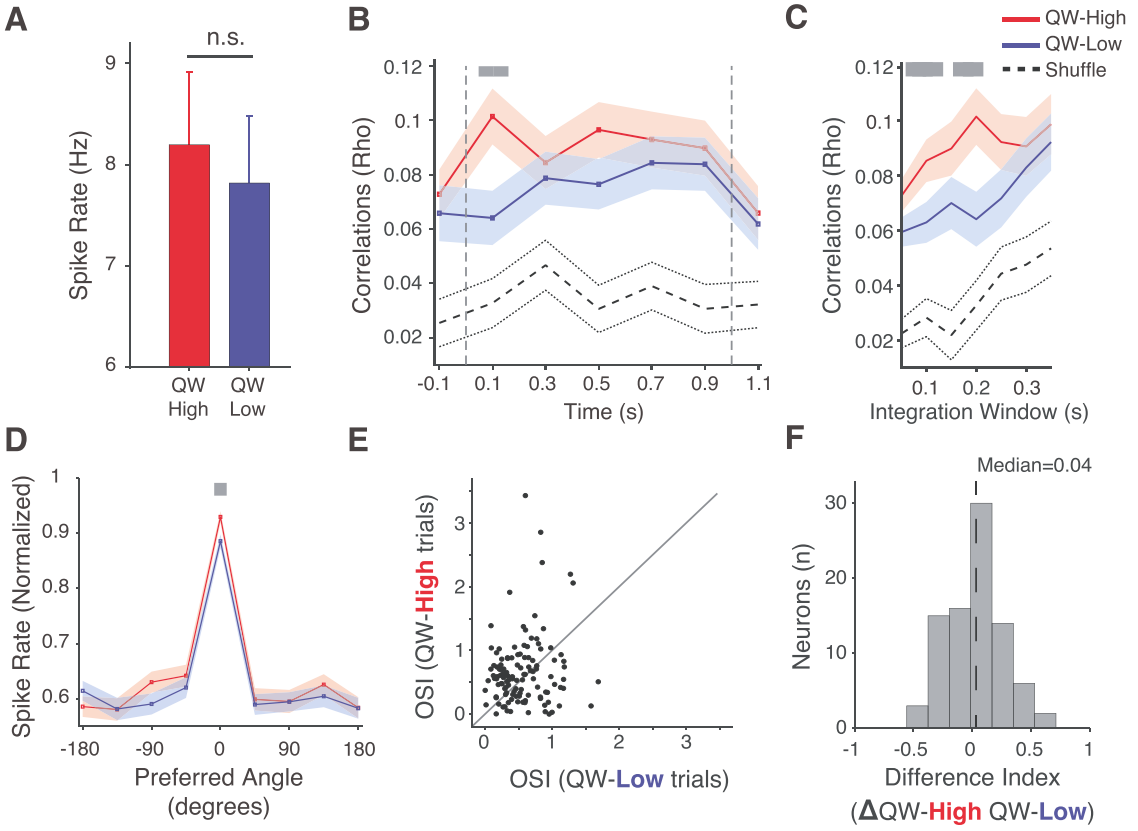

Fig. 2. Neuronal responses in primary visual cortex during high- and low-arousal quiescent states. (A) Average (± SEM) spike rate in V1 across the stimulation period (0.8 s post-stimulus onset) across all channels, sessions, and ferrets. Differences are non-significant (QW-L: 7.9 ± 0.7 Hz, QW-H: 8.2 ± 0.7 Hz, $P = 0.86$ rank-sum = 2.1 x 10^4, Wilcoxon rank-sum test). (B) Spike-count correlations (r_{SC}) as a function of time. The r_{SC} values were calculated using an integration window of 0.2 s. The red and blue lines represent the average r_{SC} values ± SEM (ribbon) across recorded neurons for high- and low-QW arousal conditions, respectively. Gray vertical dashed lines at the beginning and end of the trial represent stimulus onset and offset, respectively. Black dashed lines represent the average (±SEM) of r_{SC} between neurons, in which the condition labels were randomly shuffled. Gray bar denotes a P-value < 0.05 in a randomization test, corrected for multiple comparisons across observations. (C) Spike-count correlations calculated at 0.1 s post-stimulus onset as a function of different temporal integration windows. Gray bar and black dashed line as in panel (B). (D) Normalized spike rate (average ± SEM) as a function of the preferred orientation angle (in degrees). Gray bar denotes a P-value < 0.05 in a randomization test, corrected for multiple comparisons across observations. (E) Scatter plot of the OSI values during high- and low-arousal during QW. Each dot represents the average values of a recorded neuron. During visual stimulation, OSI values significantly increase during high arousal (QW-H) ($P = 0.023$, $z = 2.26$, sign = 48; sign test). (F) Histogram of the OSI differences between high and low QW. Positive values indicate a higher OSI during QW-high. The dashed line represents the median of the distribution (0.04). The distribution differed significantly from zero ($P = 0.03$, $z = 2.05$, rank-sum = 8591; Wilcoxon rank-sum test).

the OSI during QW-H. This increase was observed using an index of the difference across conditions of very selective neurons with high OSI values (Fig. 2F). In this analysis, positive index values indicate an increase in the OSI during high arousal. Furthermore, the difference index distribution was significantly distinct from zero ($P = 0.03$, Wilcoxon rank-sum test: $z = 2.05$, rank-sum = 8591).

In sum, these results show that high-arousal QW behavioral states increase the OSI and the spike-count correlation of the neuronal population. An increase in r_{SC} values implies an increase in the synchronized activity of neurons due to common input. Interestingly, high r_{SC} has been interpreted as a decrease in the quality of information processing (Cohen and Kohn 2011). Here we showed that, despite high r_{SC} values, QW-H improves the response selectivity of neurons in V1 during stimulus processing.

High- and low-arousal states during quiet wakefulness induce amplitude and peak shifts of the spectral power

The LFP signal is a prime candidate for studying the relationship between behavioral states and cortical microcircuit function changes. Rhythmic fluctuations of the LFP across time primarily reflect synchronized excitatory and inhibitory interactions among cortical microcircuits neurons (Buzsáki et al. 2012; Pesaran et al. 2018). Furthermore, these LFP oscillations have been associated with several cognitive functions and computational mechanisms (Fries 2009; Bosman et al. 2014; Singer 2018). Because behavioral states influence the synaptic activity of cortical microcircuits, we explored LFP power dynamics across different QW conditions during passive stimulation (Fig. 3). We recorded the LFP activity of one primary sensory area (V1) and a hierarchically superior area (area PPc), focusing on the power changes between high- vs. low-arousal quiescent periods in which animals passively observed the displayed gratings. We compared these power fluctuations with those elicited during a baseline period without stimulation.

We observed several changes in the LFP signal associated with the animal's behavioral state (Supplementary Fig. 2C–H, Fig. 3). As expected (Harris and Thiele 2011; McGinley, Vinck, et al. 2015), QW-H shows a significant decrease in the power at lower frequencies and a small but significant increase in the power at higher frequencies (Supplementary Fig. 2E–H). During visual stimulation, an inspection of the individual LFP raw traces also shows an increase in the faster rhythms during those trials with bigger pupil dilation

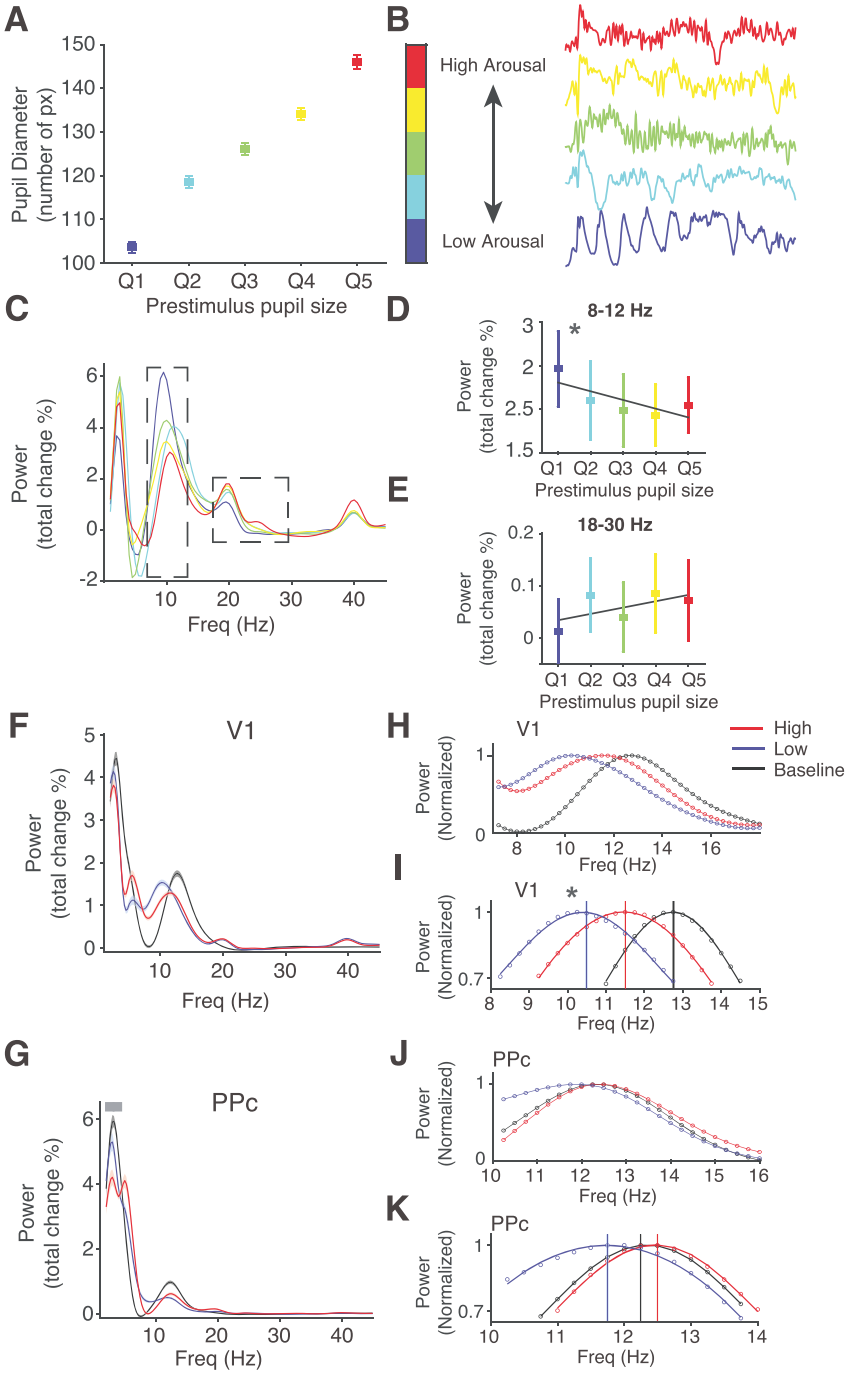

Fig. 3. LFP power estimation in primary visual and posterior parietal cortex during high- and low-arousal trials. (A) Average ± SEM of the pre-stimulus pupil sizes for each quintile. (B) Raw LFP traces from a representative electrode in V1 (1 s after visual stimulation). Trials were classified according to the pre-stimulus pupil diameter distribution, separated into quintiles. (C) Average power spectrum (% of the total power, IRASA estimation) for a representative electrode in V1, classified according to the quintiles of the pre-stimulus pupil diameter distribution. Color code according to panel (A). The frequency cut-off of the IRASA power estimation was set at 50 Hz. Dashed squares show the frequency bands analyzed in panels (D) and (E). (D) Average power spectrum estimation (% of the total power, IRASA estimation) for the alpha-frequency band (8–12 Hz) separated across quintiles. The gray asterisk denotes a significant relationship between the pupil diameter distribution quintiles and the decrease of the alpha-frequency band power ($P = 0.006$, $t\text{-stat} = -2.86$, fixed effect regression). (E) Same as (D) but for a beta-frequency band (18–30 Hz). A fixed effect regression does not show a correlation between the pupil diameter distribution quintiles and the beta power increase ($P = 0.56$, $t\text{-stat} = 0.57$, fixed effect regression). (F) Average power spectrum (% of the total power) across all channels, sessions, and ferrets in V1. Black, red, and blue traces (average ± SEM) correspond to the activity during baseline, high- and low-arousal conditions. (G) Same as (F) but for posterior parietal cortex. The gray bar shows a significant power decrease at a frequency band between 1 and 4 Hz modulated by arousal ($P = 0.036$, $\chi^2(2) = 6.65$, likelihood ratio test). (H) Individual power peaks of an 8–16 Hz frequency band in V1 for baseline (black), high- (red), and low- (blue) arousal conditions. Power values are normalized to the maximum. Scaled spectra are shown in dots. (I) A cosine function was fitted to the top third of the power for each condition ($R > 0.98$ for each curve). Vertical lines represent the peak of the frequency band. Shaded regions correspond to the 95% CI. The gray asterisk denotes a significant shift change due to arousal ($P = 0.009$, $\chi^2(2) = 9.25$, likelihood ratio test, frequency peaks: Baseline: 12.76 Hz, high arousal: 11.24 Hz, shift from baseline −1.51 ± 0.47 Hz, low arousal: 10.29 Hz, shift from baseline −2.47 ± 0.55 Hz). (J) Same as (H) but for posterior parietal cortex. (K) Same as (I) but for the posterior parietal cortex. The GLM analysis did not show statistical significance ($P = 0.07$, $\chi^2(2) = 5.61$, likelihood ratio test, frequency peaks: baseline: 12.25 Hz, high arousal: 12.51 Hz, shift from baseline: 0.26 ± 1.13 Hz, low arousal: 11.78 Hz, shift from baseline −0.47 ± 1.19 Hz).

compared with the trials with smaller ones (Supplementary Fig. 2C and D).

Previous studies have suggested that this shift between brain states reflects a functional continuum rather than qualitative differences between states. For instance, these studies have shown that membrane potential depolarization (and spike rate increases) follows parametric pupil diameter enlargements (McGinley, David, et al. 2015; Neske et al. 2019). We wondered whether we could observe a similar relationship between spectral power and spontaneous pupil fluctuation during visual stimulation. We sorted the LFP trials according to the quintile values of the pre-stimulus pupil diameter distribution (Figs. 1D, 3A and B). Then, we calculated the sustained power spectrum across all visual channels during a time window of 1 s. We considered an analysis window starting at 0.3 s post-stimulus presentation to avoid power induced by event-related changes. In the visual cortex, we found that passive stimulation induced a decrease of the power amplitude at the alpha-frequency band (8–12 Hz) (Fig. 3C shows the power spectrum of a representative channel for all quintiles. The dashed squares highlight an 8–12 and 18–30 Hz frequency band, respectively. Fig. 3F shows the average power spectrum across channels, sessions, and ferrets during baseline and visual stimulation for the 1st and 5th quintile distribution). We found a significant correlation between the average pre-stimulus pupil diameter and the reduced stimulus-induced power in the alpha-frequency band (Fig. 3D, $P = 0.006$, $t\text{-stat} = -2.86$, fixed effect regression). The same analysis revealed a non-significant correlation between a beta-frequency band (18–30 Hz) and arousal (Fig. 3E, $P = 0.56$, $t\text{-stat} = 0.57$, fixed effect regression). In conclusion, we show a parametric decrease in alpha power as a function of the pre-stimulus pupil increase, supporting the notion that changes in neural dynamics are part of a functional continuum within arousal states.

In area PPc, we also observed a power decrease between 1 and 4 Hz after the presentation of a stimulus. Notably, the power amplitude at the peak of this frequency band shows a modest but significant decrease by about $2 \pm 0.7\%$ of the total power in area PPc during QW-H (Fig. 3G, $P = 0.036$, $\chi^2(2) = 6.65$, likelihood ratio test), indicating that the state of arousal can also modulate stimulus-induced power changes at PPc during quiescent wakefulness.

We also observed a peak shift within an 8–16 Hz frequency band as a function of the arousal state in V1 but not in area PPc (Fig. 3H–K). To estimate the peak value for each condition and area, we scaled the spectra and fitted a cosine to the upper third of the band (Fig. 3I and K, all R values > 0.99). We used a mixed model with the arousal conditions as a predictor to evaluate the statistical significance of this spectral shift. In V1, visual stimulation induced a significant shift of the power peak towards lower frequencies. In addition, QW-L shifted the peak towards lower frequencies compared with high arousal (see Fig. 3H for the entire power spectrum comparison and Fig. 3I for the peak differences; $\chi^2(2) = 9.25$ $P = 0.009$, likelihood ratio test. Frequency peaks per group: baseline: 12.76 Hz; high arousal: 11.24 Hz, shift from baseline: -1.51 ± 0.47 Hz; low arousal: 10.29 Hz, shift from baseline: -2.47 ± 0.55 Hz). In contrast, neither visual stimulation nor QW states induced significant power peak changes in area PPc (Fig. 3J and K; $\chi^2(2) = 5.61$ $P = 0.07$, likelihood ratio test. Frequency peaks: baseline: 12.25 Hz, high arousal: 12.51 Hz, shift from baseline: 0.26 ± 1.13 Hz, low arousal: 11.78 Hz, shift from baseline -0.47 ± 1.19 Hz).

High- and low arousal conditions are differentially coupled to frequency-dependent interareal coherence

Behavioral states are considered global phenomena (Harris and Thiele 2011) with uniform neural underpinnings across different brain areas. However, previous studies have stressed that functional connectivity at macroscopic and microscopic levels depends on anatomical connectivity and behavioral state (Crochet and Petersen 2006; Poulet and Petersen 2008; Olcese et al. 2016, 2018; Poulet and Crochet 2019). Our power amplitude analyses suggest low- and high-arousal states during QW elicit different power frequency band signatures in visual and parietal cortices. Therefore, we wondered whether visual and parietal cortices show similar or different functional connectivity profiles during QW. We used the WPLI index, which measures the phase consistency across 2 oscillatory signals, correcting for volume conduction (see Section Methods), as an estimate of the functional communication within and between visual and parietal channels (Fig. 4, all significant results obtained with $P < 0.05$ using a nonparametric randomization test corrected by multiple comparisons, see Section Methods).

The average WPLI spectrum across channels within the visual cortex showed a significantly increased narrow band centered at 40 Hz during high arousal relative to low arousal (Fig. 4A). Conversely, we observed a significant increase of the WPLI at 4–8 Hz in the parietal cortex during high arousal (Fig. 4B). When we evaluated the WPLI spectrum across areas, we observed that a similar 4–8 Hz increase during high arousal dominated functional connectivity between areas (Fig. 4C).

Our WPLI results suggest that functional connectivity increases during high arousal but with a different spectral profile depending on the area. Enhanced low-frequency WPLI is observed within and between PPC and the visual cortex. In contrast, WPLI within V1 showed an increase in gamma-band synchronization. Our results show that the functional connectivity between brain areas in the ferret resembles that observed in the visual cortical system of non-human primates (van Kerkoerle et al. 2014; Bastos et al. 2015), possibly reflecting hierarchical relationships between brain regions (Markov et al. 2014).

Simulation of functional connectivity patterns by a computational model

Inter- and intra-area anatomical connections carry feedback (FB) and feedforward (FF) information targeting specific laminar compartments, depending on the hierarchical level of sending and receiving areas (Markov et al. 2013). Therefore, we wondered whether the observed differences in connectivity between high- and low-arousal states during QW can be simulated by differentially modulating the activity of the cortical laminae. We modified a previously developed large-scale computational model constrained by weighted connectivity data derived from the macaque cortex (Mejias et al. 2016), testing different FB connectivity profiles between V1 and PPc (Supplementary Figs. 3 and 4; Figs. 5A and 6, see Section Methods for a model description).

We produced 680 LFP epochs of 2 s duration organized in 4 "channels" (2 channels in area V1 and 2 in area PPc, Supplementary Fig. 3A). The power spectrum obtained from the model shows 2 well-defined peaks at alpha- and gamma-frequency bands for both conditions (Supplementary Fig. 3C and D). Fig. 5B shows the WPLI index estimation obtained from the model architecture depicted in Fig. 5A. Supplementary Fig. 3D–F shows

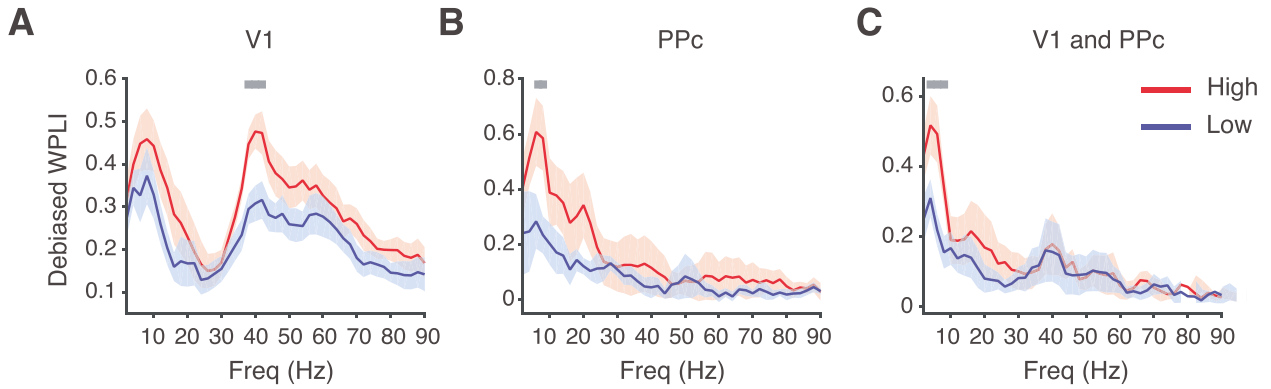

Fig. 4. Intra- and inter-areal coherence between primary visual and parietal cortices during visual stimulation increases during a high-arousal quiescent state. (A) WPLI (squared WPLI debiased, a measure for LFP–LFP phase-locking connectivity, see Section Methods) for all channel combinations in V1 (average ± SEM) and high- (red) and low- (blue) arousal conditions. The gray bar shows a $P < 0.05$ level corrected for multiple comparisons across frequencies (nonparametric randomization test across site pairs; see Section Methods). A significant increase of the WPLI index, centered at a narrow gamma-frequency band (40–50 Hz), is observed during high-arousal quiescent states. (B) Same as (A) but for channel pairs within the posterior parietal cortex. (C) Same as (A) but for channel pairs between V1 and posterior parietal cortex. In (B) and (C), a significant increase of the WPLI, centered around a theta-frequency band (4–8 Hz), is observed during high-arousal quiescent states.

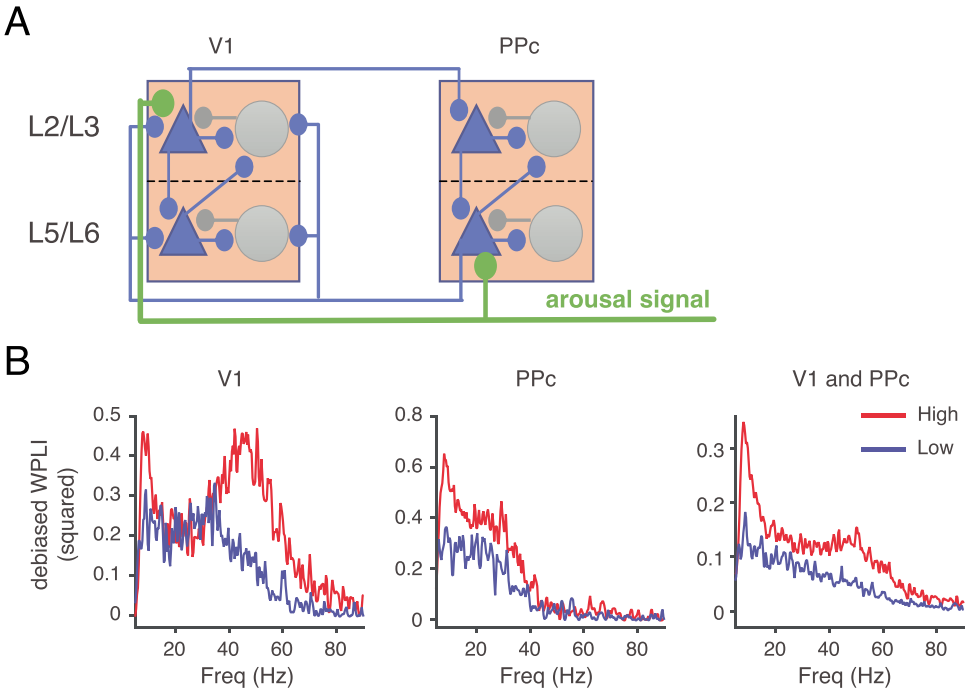

Fig. 5. A computational model that resembles the WPLI coherence observed between V1 and PPc. (A) Schema of the interlaminar circuit used to model the results observed in Fig. 4. A simplified, minimal model, or a cortical column that describes the laminar-specific interactions between V1 and PPc and the influence of FB signals on them. In green, top–down projections carry arousal signals to the supragranular compartment of V1 and the infragranular compartment of PPc. (B) Computational prediction of the functional connectivity, measured as WPLI-debiased index, within area V1 (left panel), within area PPc (middle panel), and between area V1 and PPc (right panel). Color codes are the same as in Fig. 4. The configuration depicted in Fig. 5A approximates the results observed in Fig. 4 (see Table 1 for the model parameters).

the coherence spectra estimates of the model. These coherence results constitute a model prediction for future studies, while results from WPLI can be directly compared with our existing data. We assumed that arousal signals are conveyed by excitatory FB projections targeting the infragranular layers of PPc and supragranular layers of V1, thus allowing the replication of the above-mentioned functional connectivity results. Our model establishes layer-specific FB modulations as a potential mechanistic implementation of arousal signals to the visual and parietal cortex during different quiescent states. Importantly, the model does not inform us about the origin of such modulatory signals, which can be traced back to subcortical neuromodulatory signals or cortico-cortical FB projections, for example (see Section Discussion).

We have also studied the predictions of our model when other types of laminar FB projections are considered. Figure 6 compares 5 different connectivity patterns between infra- and supragranular layers and the estimated WPLI spectra for intra- and inter-area connectivity. Figure 6A duplicates the model from Fig. 5. It compares it with 4 alternative scenarios with different ratios for infra/supra granular FB intensities (Fig. 6B–E, see Supplementary Fig. 3 for the coherence spectra estimates of the same models). These alternative models resemble some but not all features of the observed data. For example, the alternative model offered in

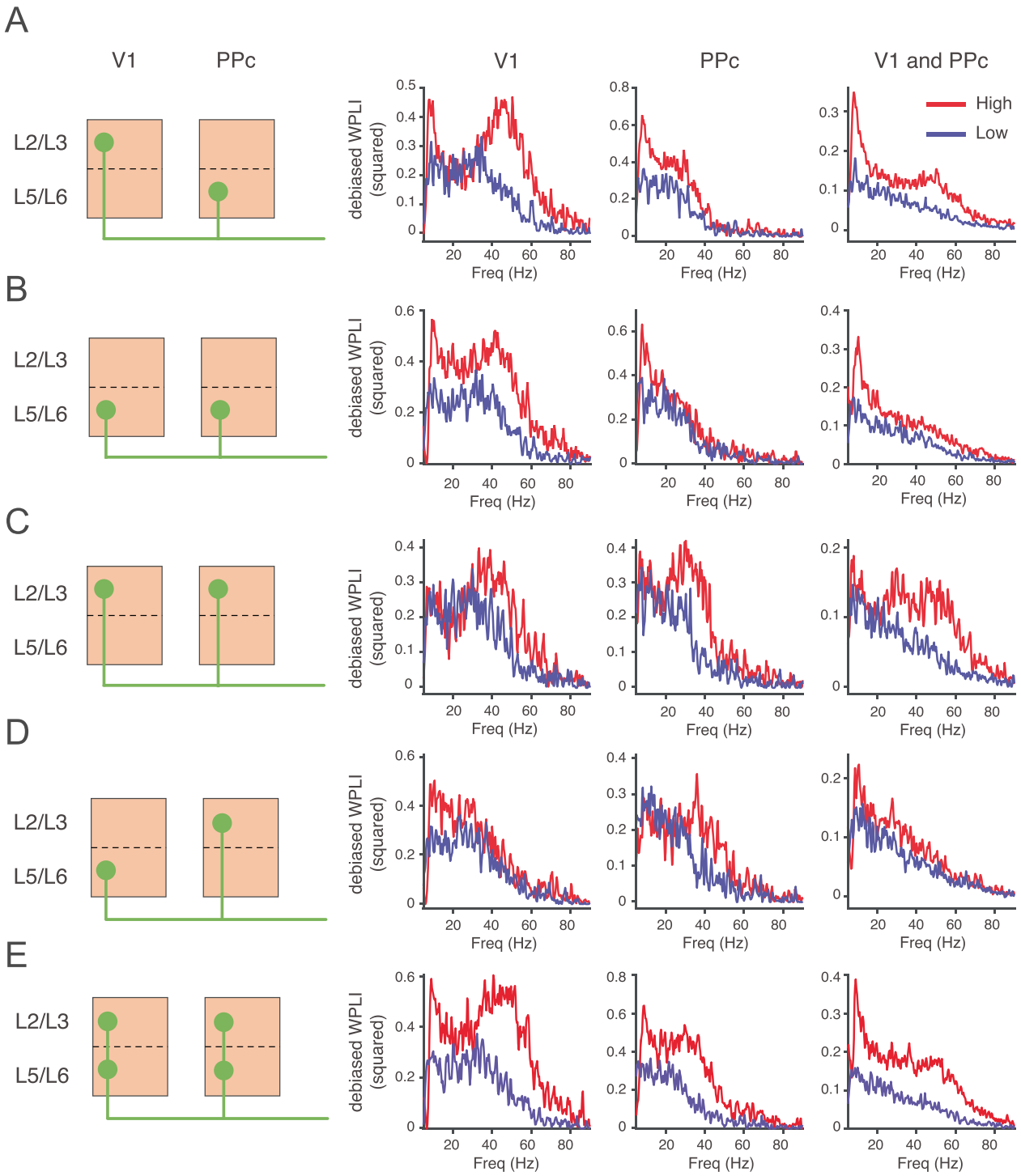

Fig. 6. Inter- and intra-area coherence estimates vary according to the pattern of interlaminar projections. (A–E) Left: variations in interlaminar FB projection patterns used to test the functional connectivity model. Right: WPLI spectra of the functional connectivity within and between the primary visual cortex and PPc (plotting conventions as in Fig. 4). Panel A is the same as used in Fig. 5.

Fig. 6B (i.e. FB preferentially targeting deep layers of both cortical areas) provides a plausible alternative that shows a reduced gamma peak in V1-PPC interactions under low-arousal conditions (in line with experimental data), but at the expense of an increased alpha peak for V1, which we did not find in the data. Alternative models are shown in Fig. 6C (FB to superficial layers), Fig. 6D (FB to superficial layers of PPC and deep layers of V1), and Fig. 6E (simultaneous FB to supra and infragranular layers). Interestingly, the simultaneous FB towards supra and infragranular layers qualitatively reproduces some of the features observed in our original model. However, this FB configuration does not consider the anatomical asymmetry of top–down projections across different brain regions (Markov et al. 2014). Thus, these models cannot reproduce the observed results or the anatomical configuration of top–down projections and are therefore less plausible explanations. A balanced FB modulation through excitatory projections to supragranular and infragranular layers in primary visual and PPc cortices, respectively, is thus best consistent with

our experimental findings on functional connectivity during high- and low-arousal quiescent.

In sum, our model establishes layer-specific FB as a possible mechanistic implementation of arousal latter signals to the visual and parietal cortex. Furthermore, the FB structure considered in this model is compatible with current hypotheses about the hierarchical distance of FB generation signals and targeting downstream areas (Markov et al. 2013, 2014; Harris et al. 2019), suggesting potential parallelisms between FB modulations in ferrets and macaques.

Narrow and broad spiking V1 cells phase-lock to different frequency bands during quiescent high-arousal conditions

Because excitatory and inhibitory neurons entrain to local rhythms at distinct phases of the oscillatory period, with functional implications for cortical microcircuits (Hasenstaub et al. 2005; Siegle et al. 2014; McGinley, Vinck, et al. 2015; Vinck et al. 2016), we evaluated whether different neuronal populations specifically phase-lock to the observed LFP rhythms during high and low QW conditions. First, we sorted the 110 visually responsive neurons in V1 using the peak-to-trough duration of their waveform (Fig. 7A) (Mitchell et al. 2007; Lansink et al. 2010; Vinck et al. 2016; Arbab et al. 2018). The distribution of peak-to-trough values was significantly bimodal ($P = 0.03$, Hartigan's dip test: dip = 0.04). Then, we selected narrow-spiking and broad-spiking cells using 350 μs of the peak-to-trough duration as a criterion for separation. Using this procedure, we obtained 17 narrow-spiking and 84 broad-spiking cells. Nine neurons remained unclassified (Fig. 7B).

Next, we quantified the phase-locking consistency of the spikes from these 2 populations to the underlying LFP rhythm using the pairwise phase consistency (PPC) index across frequencies (Vinck et al. 2012). We observed that narrow and broad-spiking cells significantly increased their phase locking to different brain rhythms during QW-H. Narrow-spiking cells are simultaneously locked to an alpha (11–15 Hz) and a gamma- (60–70 Hz) frequency band (Fig. 7C, 11–15 Hz and 60–70 Hz, $P < 0.05$ permutation test). In contrast, broad-spiking cells are only phase-locked to the 60–70 Hz gamma-frequency band (Fig. 7E, 60–70 Hz, $P < 0.05$ permutation test). Figure 7D and F shows the PPC average across the population of cells to these bands (Fig. 7D, exact Mann–Whitney U test: narrow-spiking population: alpha-frequency band: $P = 0.003$, $U = 2989$; gamma-frequency band: $P = 0.001$, $U = 3030$; broad-spiking population: alpha-frequency band: $P = 0.95$, $U = 53{,}920$; gamma-frequency band: $P = 0.005$, $U = 62{,}179$). These results suggest that high- and low-frequency brain rhythms distinctively influence the activity of visual cortex neurons during high-arousal states, with low-frequency phase locking reflecting the engagement of narrow-spiking cells to an alpha rhythm that is likely associated with top–down modulation (Arnal et al. 2011; van Kerkoerle et al. 2014; Bastos et al. 2015).

Discussion

Our results indicate that the spontaneous arousal levels, gauged via pre-stimulus pupil variability, affect post-stimulus neuronal processing during quiescence in head-fixed ferrets passively observing visual stimuli. The pupil size of these ferrets showed spontaneous fluctuations over time (Fig. 1), which seemed to correlate with different levels of arousal (Reimer et al. 2014; McGinley, David, et al. 2015; McGinley, Vinck, et al. 2015; Vinck et al. 2015; Einstein et al. 2017; Neske et al. 2019). When trials were grouped according to pre-stimulus pupil dilation, we observed that neurons in V1 increased their firing rate at their preferred orientation during high-arousal states (Fig. 2). Also, the LFP power amplitude shifted from a preeminence of low-frequency bands to higher frequencies. Stimulus onset shifted the peak of an alpha band (~12 Hz) towards lower frequencies, but the magnitude of the peak shift depended on the arousal state (Fig. 3). High arousal increased LFP–LFP phase relationships at lower frequencies within and between the visual and parietal cortices (Fig. 4). A computational model mimicking a laminar architecture receiving FB from emulating arousal signals between V1 and PPC showed that this spectral signature is compatible with FB from higher cortical areas targeting infragranular layers in PPc and supragranular layers in V1 (Figs. 5 and 6). Finally, we observed narrow and broad-spiking neurons phase-locking to different LFP rhythms when stimulated during high arousal. Broad-spiking neurons entrained to high-frequency oscillations (>60 Hz), whereas narrow-spiking neurons phase-locked to low- (12–18 Hz) and high-frequency (50–80 Hz) rhythms (Fig. 7C and E).

Inactive to active states follow incremental changes in the variability and sensitivity of neuronal responses

Neuronal correlates of wakefulness have been studied in well-defined behavioral states of the sleep–wake cycle and during physical activity such as locomotion (Harris and Thiele 2011; McGinley, Vinck, et al. 2015; Olcese et al. 2016; Poulet and Crochet 2019). Active behavioral states produce a cortical desynchronization with a predominance of high-frequency oscillations, an increase in the variability of the neuronal activity, and an increase in the sensitivity of neurons in responding to sensory stimuli (Crochet and Petersen 2006; Gentet et al. 2010; Zagha et al. 2013; Reimer et al. 2014; McGinley, David, et al. 2015; Vinck et al. 2015, 2016; Poulet and Crochet 2019). Conversely, low-arousal states correlate with a general cortical synchronization, a prevalence of low-frequency rhythms, and decreased spike variability (Steriade et al. 1993, 2001; Amzica and Steriade 1997; Vyazovskiy et al. 2011; McCormick et al. 2014; Sanchez-Vives et al. 2017). QW shows similar but dampened features as those observed during locomotion or attention (Reimer et al. 2014; McGinley, Vinck, et al. 2015; Neske et al. 2019; Poulet and Crochet 2019), and recent studies have proposed that transitions from inactive to active states follow incremental changes in the variability and sensitivity of neuronal responses (McGinley, David, et al. 2015; Neske et al. 2019). This monotonic increase with arousal suggests the existence of a continuum between the range of neuronal responses and wakefulness states. For example, in humans, recent studies have used pupil size to characterize brain signatures of arousal fluctuations during the waking states during task performance or rest (de Gee et al. 2021; Mäki-Marttunen 2021; Wainstein et al. 2021; Lee et al. 2022) showing that these arousal fluctuations correlate with similar brain's functional integration changes. In agreement with these findings, we found that the alpha-frequency band power elicited during visual stimulation parametrically decreases as a function of arousal. Altogether, these results support the notion that pre-stimulus wakefulness affects neuronal responses to stimuli processing.

Our study focused on the trials with the smallest and largest pupil diameter size during QW and determined that these 2 conditions unveil quantitative differences in neuronal sensitivity as a function of arousal in the ferret. High-arousal QW increased stimulus selectivity in orientation-selective neurons in line with

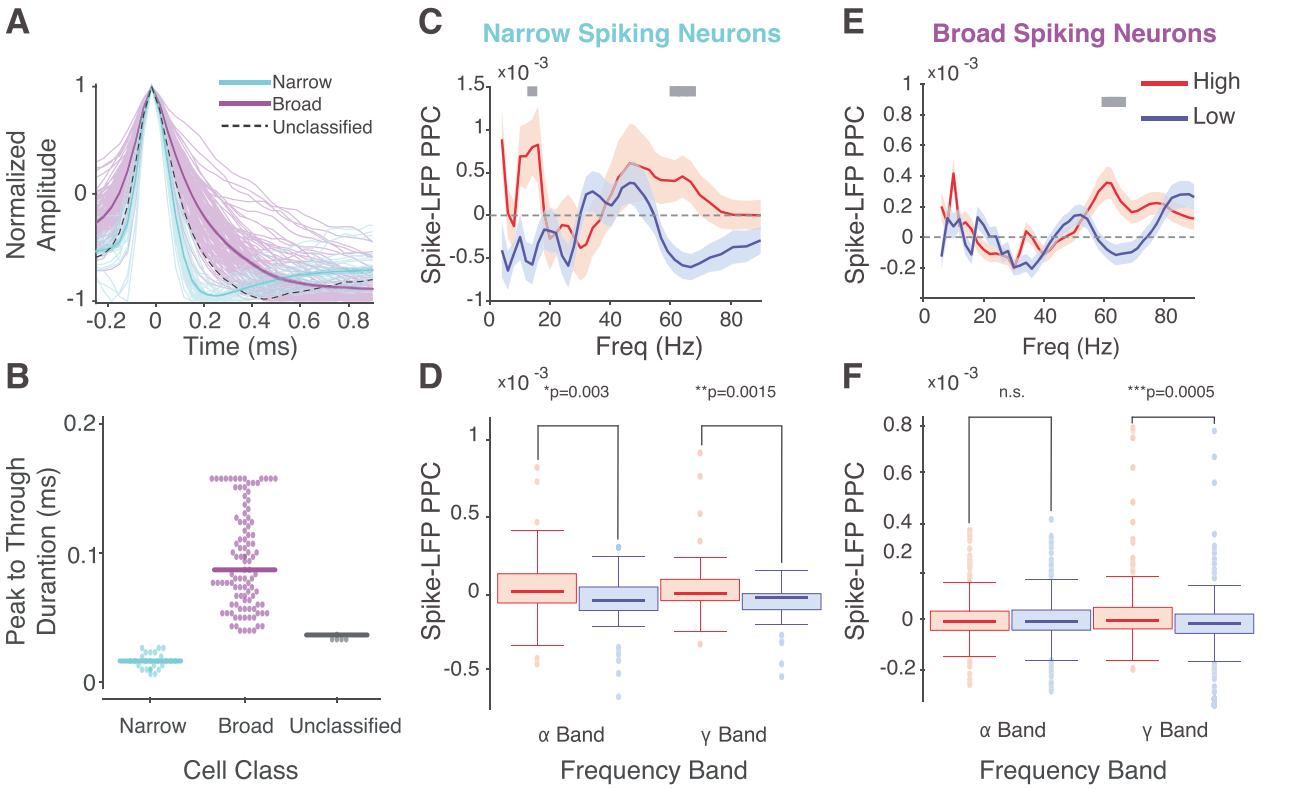

Fig. 7. Spike-LFP phase coherence in primary visual cortex. Narrow- and broad-spiking cells increase their phase locking to alpha- and gamma-frequency band during high-arousal quiescent states. (A) Normalized spike waveform amplitude as a function of time (ms) for action potentials of neurons sorted by peak-to-trough-duration. Narrow (cyan), broad (violet), and unclassified (dashed line) spiking cells. Thick lines and ribbon area correspond to the average ± SEM, respectively. (B) Beeswarm plot of the neuronal cell types, with the horizontal line representing the median of each group. The observed distribution of the dots was bimodal ($P = 0.03$, dip = 0.04, Hartigan's dip test). (C) PPC spectrum of narrow-spiking cells sorted across high- (red) and low-QW (blue) arousal conditions. Average across V1 channels and narrow-spiking neurons ± SEM (ribbon). Gray bars denote $P < 0.05$ corrected for multiple comparisons across frequencies, nonparametric randomization test. (D) Box plot of PPC differences of narrow-spiking cells per band (alpha and gamma, based on the differences observed in panel (C) as a function of the high- and low-arousal conditions (significance threshold: $P < 0.05$, Wilcoxon's rank-sum test). (E) Same as (C) but for broad-spiking cells. (F) Same as (D) but for broad-spiking cells.

what was previously observed during locomotion compared with rest (Niell and Stryker 2010; Vinck et al. 2015) and QW compared with anesthesia (Ecker et al. 2014; Reimer et al. 2014). This sensitivity change of neurons in the primary visual cortex is not induced by a general increase in the spike rate (Fig. 2A), a finding also observed in previous reports (Vinck et al. 2015; Poulet and Crochet 2019). Instead, we observed that these changes are associated with spike-count correlation differences among neurons (Fig. 2B and C), together with changes in power amplitude and phase synchrony of the LFP signal.

The spike-count correlation accounts for the shared variability between pairs of 2 recorded neurons (Cohen and Kohn 2011). In the ferret primary visual cortex, we found that the shared variability across neurons transiently increases immediately after stimulus onset during high-arousal trials. This contrasts with previous studies showing a decrease in shared variability of spiking responses after stimulus onset (Renart et al. 2010; Renart and Machens 2014; Neske et al. 2019; Waschke et al. 2021). However, spike-count correlations can also change as a function of wakefulness state, attention, or anesthesia (Reimer et al. 2014; Ruff and Cohen 2014; Snyder et al. 2014; Denfield et al. 2018), depending on the heterogeneity of the population under examination (Ecker et al. 2011; Arbab et al. 2018). Because neurons with similar orientation properties tend to have a higher degree of shared variability (Pachitariu et al. 2015), the transient high-arousal post-stimulus increase in spike-count correlations might reflect neurons with similar tuning properties. Moreover, we confirmed previous observations in V1 that describe a shift of the LFP power with increasing arousal levels (Crochet and Petersen 2006; Gentet et al. 2010; Bennett et al. 2013; Polack et al. 2013; Zagha et al. 2013; Reimer et al. 2014; Schneider et al. 2014; McGinley, David, et al. 2015; Vinck et al. 2015; Einstein et al. 2017; Fernandez et al. 2017; Stitt et al. 2018). After stimulus onset, we detected a peak shift of the alpha-frequency band (~11–15 Hz) towards lower frequencies in the primary visual cortex (Fig. 3). The magnitude of the shift depended on the wakefulness state of the animal (Fig. 3H and I). The occipital alpha peak increases the frequency when subjects switch from passive viewing to an active cognitive task (Haegens et al. 2014). We found that while visual stimulation reduces the frequency peak of alpha power (Fig. 3I), QW-H shows consistently higher alpha peaks than QW-L. Previous studies on gamma oscillations have found that this peak variability might reflect rapid cyclic changes in synaptic excitation (and a proportional inhibitory counterbalance) within a cortical microcircuit (Atallah and Scanziani 2009; Spyropoulos et al. 2022). Our results show that this variability can also affect low-frequency oscillatory components of the LFP.

Earlier studies have identified the activity of infragranular cortical layers and their thalamic modulation as the probable cortical source of alpha rhythms (Lopes da Silva and Leeuwen 1977; Lopes da Silva et al. 1980). This thalamic modulation sustains cortical connectivity during attentional states in

primates and rodents (Saalmann et al. 2012; Schmitt et al. 2017). In ferrets, theta and alpha rhythms modulate the communication between the thalamus and area PPc depending on the wakefulness state of the animal (Stitt et al. 2018). We did not observe such parietal modulations, but unaltered responses in other cortical layers may have masked them. Future studies using brain-wide recording techniques might elucidate these questions.

Intra- and inter-areal phase synchronization fluctuates during quiescent wakefulness.

Consistent local and long-range LFP–LFP phase relationships between areas associated with cognitive tasks have been described in several species (Bosman et al. 2014; Fries 2015; Vinck et al. 2016). This study found that a low-frequency band component dominates the intraparietal (Fig. 4B) and parietal–visual LFP–LFP phase relationships (Fig. 4C). This increase of low-frequency synchronization strength in periods of high arousal is in line with previous findings (Vyazovskiy et al. 2011; Olcese et al. 2016, 2018; Fernandez et al. 2017), but in addition to that, we observed in V1 an increase in coherence (WPLI) in a narrow gamma-frequency band. This narrow gamma band (between 40 and 60 Hz) might represent the functional interaction between the primary visual cortex and the lateral geniculate nucleus, which also depends on the arousal state of the animal (Saleem et al. 2017; Schneider et al. 2021). Our results reveal frequency-specific influences between areas depending on the wakefulness state of the animal. In the primate cortex, gamma influences have been reported to be systematically stronger in the feedforward direction. In contrast, alpha and beta typically dominate in the FB direction, and this organization is consistent with anatomical projection patterns (Bastos et al. 2015, see Schneider et al. 2021 for an alternative explanation). We used a model that mimicked these frequency-specific interactions across areas. Our model suggests that frequency-specific interactions, and the effects of different arousal levels on such interactions, can be captured by straightforward firing-rate models with laminar connectivity (Mejias et al. 2016). The model predicts that top–down arousal signals target deep layers of PPc and superficial layers of V1. The modeling results are consistent with existing neuroanatomical connectivity patterns of the macaque cortex (Markov et al. 2013, 2014): specific layers receiving top–down FB projections depend on the hierarchical distance between source and target, with short/long hierarchical distances corresponding to deep/superficial layers, respectively. This cortical organization successfully explains the observed local and long-range functional connectivity interactions.

Besides modeling a probable mechanistic origin of the observed frequency-dependent interactions between visual and parietal areas, our computational model provides additional information regarding arousal signals. Assuming that the influence of high-arousal states on visual and parietal areas is conveyed via top–down signals from higher cortical areas, subcortical structures (e.g. thalamus), or neuromodulatory signals (Herrero et al. 2008), we have studied frequency-specific patterns emerging for different FB configurations. Anatomical projections from higher to lower brain areas tend to be diffuse and unspecific (Markov et al. 2014). A computational model like this one facilitates the exploration of specific projections that might play a role in the emergence of the observed dynamics. Of the 5 FB types considered (Fig. 6), FB targeting deep layers of proximal areas (here: PPc) and superficial layers on distal areas (here: V1) can replicate the most notable features of the data, except for overestimating gamma oscillations in visual–parietal influences during high arousal. Both connectivity patterns include FB to deep layers (Fig. 6E). FB connections targeting deep layers for both proximal and distal areas can correct this overestimation at the expense of deviating from the data in the low-frequency range for interactions within visual neurons (Fig. 6B). Previous models have shown the importance of these FB signals during top–down inhibition (Mejias et al. 2016), and realistic distributed representations during working memory (Mejías and Wang 2022), both being essential concepts for predictive coding principles (Pennartz et al. 2019). Interestingly, these 2 FB patterns are in line with the ones observed in FB projections in the macaque cortex (Markov et al. 2014) and mice (Harris et al. 2019), respectively. Our modeling results point to the hypothesis that cortical FB in ferrets can include both scenarios, supporting a body of literature highlighting features that the ferret cortex share with that of macaques and mice (Kaschube et al. 2010; Kaschube 2014).

Neuronal entrainment to the low- and high-frequency LFP components during quiescent high-arousal reveals different modulatory effects over cortical microcircuits

Finally, we characterized the entrainment of primary visual cortex cell types, sorted according to their spike waveforms, to the observed cortical rhythms. We showed that putative excitatory and inhibitory neurons increase their entrainment to the LFP during high arousal (Polack et al. 2013; Vinck et al. 2015). In addition, while broad-spiking cells (putative pyramidal neurons) phase-locked to high-frequency oscillations, narrow-spiking cells (putative interneurons) interacted with both high- (60–70 Hz) and low-frequency (10–15 Hz) oscillations. This phase-locking pattern is consistent with the role of narrow-spiking interneurons controlling cortical microcircuit computations (Isaacson and Scanziani 2011) and the generation of high-frequency oscillations (Cardin et al. 2009; Sohal et al. 2009; Veit et al. 2017). It has recently been observed that specific parvalbumin-expressing interneurons' action might mediate cholinergic modulations within a cortical microcircuit (Garcia-Junco-Clemente et al. 2019). A subset of GABergic interneurons expressing the neuro-derived neurotrophic factor L1 receive cortico-cortical projections from neighboring microcircuits and control the gain of excitatory cells. These interneurons directly inhibit the apical dendrite of excitatory neurons while disinhibiting their somata via parvalbumin-expressing interneurons (Cohen-Kashi-Malina et al. 2021). We hypothesize that the low-frequency entrainment of narrow-spiking cells observed in our data might reflect the mediation of several cortical and subcortical influences that arousal exerts over cortical microcircuits (Harris and Thiele 2011). Future studies must elucidate the role of the interneurons during QW.

In conclusion, our results show that the variability and sensitivity of cortical responses to a stimulus critically depend on the animal's behavioral state before stimulus onset. Arousal states modulate intra- and inter-areal coherence among circuits, engaging local circuits with different LFP rhythms. Our analysis of high- and low-arousal QW states supports the notion that behavioral states are associated with continuous changes in neuronal activity and dynamics across time and provide further evidence that the variability observed during visual processing depends on the behavioral state before the stimulation.

Acknowledgments

The authors want to thank the members of the Technology Center of the University of Amsterdam for their help in building the electrophysiological setup.

Supplementary material

Supplementary material is available at *Cerebral Cortex* online.

Authors' contribution

Lianne Klaver (Conceptualization, Data curation, Formal analysis, Investigation, visualization, Writing—original draft, Writing—review & editing), Lotte Brinkhof (Data curation, Formal analysis), Tom Sikkens (Data curation, Formal analysis), Lorena Casado-Román (Data curation, Formal analysis), Alex Williams (Data curation), Laura van Mourik-Donga (Data curation), Jorge Mejias (Formal analysis, Methodology, Software, Writing—review & editing), Cyriel Pennartz (Resources, Supervision, Writing—review & editing), Conrado Bosman (Conceptualization, Formal analysis, visualization, Funding acquisition, Project administration, Resources, Supervision, Writing—original draft, Writing—review & editing)

Funding

FLAG-ERA Joint Transnational Call (JTC)-2015 (project CANON) and JTC-2019 (project DOMINO) co-financed by the Netherlands Organization for Scientific Research (Nederlandse Organisatie voor Wetenschappelijk Onderzoek, NWO) to CAB, and the European Union's Horizon 2020 Framework Program for Research and Innovation (grant numbers 720270—Human Brain Project SGA1 to CMAP, 785907—Human Brain Project SGA2 to CAB and CMAP, and 945539—Human Brain Project SGA3 to CMAP).

Conflict of interest statement: The authors report no conflict of interest.

Data availability

Data from the current study will be made available to qualified investigators upon reasonable request to the corresponding author.

References

Amzica F, Steriade M. Cellular substrates and laminar profile of sleep K-complex. *Neuroscience*. 1997:82:671–686.

Arbab T, Battaglia FP, Pennartz CMA, Bosman CA. Abnormal hippocampal theta and gamma hypersynchrony produces network and spike timing disturbances in the Fmr1-KO mouse model of fragile X syndrome. *Neurobiol Dis*. 2018:114:65–73.

Arieli A, Sterkin A, Grinvald A, Aertsen A. Dynamics of ongoing activity: explanation of the large variability in evoked cortical responses. *Science*. 1996:273:1868–1871.

Arnal LH, Wyart V, Giraud A-L. Transitions in neural oscillations reflect prediction errors generated in audiovisual speech. *Nat Neurosci*. 2011:14:797–801.

Aston-Jones G, Cohen JD. An integrative theory of locus coeruleus-norepinephrine function: adaptive gain and optimal performance. *Annu Rev Neurosci*. 2005:28:403–450.

Atallah BV, Scanziani M. Instantaneous modulation of gamma oscillation frequency by balancing excitation with inhibition. *Neuron*. 2009:62:566–577.

Averbeck BB, Lee D. Neural noise and movement-related codes in the macaque supplementary motor area. *J Neurosci*. 2003:23:7630–7641.

Averbeck BB, Lee D. Effects of noise correlations on information encoding and decoding. *J Neurophysiol*. 2006:95:3633–3644.

Bastos AM, Vezoli J, Bosman CA, Schoffelen J-M, Oostenveld R, Dowdall JR, Weerd PD, Kennedy H, Fries P. Visual areas exert feedforward and feedback influences through distinct frequency channels. *Neuron*. 2015:85:390–401.

Bennett C, Arroyo S, Hestrin S. Subthreshold mechanisms underlying state-dependent modulation of visual responses. *Neuron*. 2013:80:350–357.

Berens P, Keliris GA, Ecker AS, Logothetis NK, Tolias AS. Comparing the feature selectivity of the gamma-band of the local field potential and the underlying spiking activity in primate visual cortex. *Front Syst Neurosci*. 2008:2:2.

Bosman CA, Lansink CS, Pennartz CMA. Functions of gamma-band synchronization in cognition: from single circuits to functional diversity across cortical and subcortical systems. *Eur J Neurosci*. 2014:39:1982–1999.

Brainard DH. The psychophysics toolbox. *Spat Vis*. 1997:10:433–436.

Buzsáki G, Anastassiou CA, Koch C. The origin of extracellular fields and currents - EEG, ECoG, LFP and spikes. *Nat Rev Neurosci*. 2012:13:407–420.

Cardin JA, Carlén M, Meletis K, Knoblich U, Zhang F, Deisseroth K, Tsai L-H, Moore CI. Driving fast-spiking cells induces gamma rhythm and controls sensory responses. *Nature*. 2009:459:663–667.

Cohen MR, Kohn A. Measuring and interpreting neuronal correlations. *Nat Neurosci*. 2011:14:811–819.

Cohen MR, Maunsell JHR. Attention improves performance primarily by reducing interneuronal correlations. *Nat Neurosci*. 2009:12:1594–1600.

Cohen-Kashi-Malina K, Tsivourakis E, Kushinsky D, Apelblat D, Shtiglitz S, Zohar E, Sokoletsky M, Tasaka G, Mizrahi A, Lampl I, et al. NDNF interneurons in layer 1 gain-modulate whole cortical columns according to an animal's behavioral state. *Neuron*. 2021:109:2150–2164.e5.

Crochet S, Petersen CCH. Correlating whisker behavior with membrane potential in barrel cortex of awake mice. *Nat Neurosci*. 2006:9:608–610.

de Gee JW, Correa CMC, Weaver M, Donner TH, van Gaal S. Pupil dilation and the slow wave ERP reflect surprise about choice outcome resulting from intrinsic variability in decision confidence. *Cereb Cortex*. 2021:31:bhab032.

Dell L, Innocenti GM, Hilgetag CC, Manger PR. Cortical and thalamic connectivity of posterior parietal visual cortical areas PPc and PPr of the domestic ferret (Mustela putorius furo). *J Comp Neurol*. 2019:527:1315–1332.

Denfield GH, Ecker AS, Shinn TJ, Bethge M, Tolias AS. Attentional fluctuations induce shared variability in macaque primary visual cortex. *Nat Commun*. 2018:9:2654.

Ecker AS, Berens P, Keliris GA, Bethge M, Logothetis NK, Tolias AS. Decorrelated neuronal firing in cortical microcircuits. *Science*. 2010:327:584–587.

Ecker AS, Berens P, Tolias AS, Bethge M. The effect of noise correlations in populations of diversely tuned neurons. *J Neurosci*. 2011:31:14272–14283.

Ecker AS, Berens P, Cotton RJ, Subramaniyan M, Denfield GH, Cadwell CR, Smirnakis SM, Bethge M, Tolias AS. State dependence of

noise correlations in macaque primary visual cortex. *Neuron*. 2014:82:235–248.

Einstein MC, Polack P-O, Tran DT, Golshani P. Visually evoked 3–5 Hz membrane potential oscillations reduce the responsiveness of visual cortex neurons in awake behaving mice. *J Neurosci*. 2017:37:5084–5098.

Fernandez LMJ, Comte J-C, Merre PL, Lin J-S, Salin PA, Crochet S. Highly dynamic spatiotemporal organization of low-frequency activities during behavioral states in the mouse cerebral cortex. *Cereb Cortex*. 2017:27:5444–5462.

Fries P. Neuronal gamma-band synchronization as a fundamental process in cortical computation. *Annu Rev Neurosci*. 2009:32:209–224.

Fries P. Rhythms for cognition: communication through coherence. *Neuron*. 2015:88:220–235.

Garcia-Junco-Clemente P, Tring E, Ringach DL, Trachtenberg JT. State-dependent subnetworks of parvalbumin-expressing interneurons in neocortex. *Cell Rep*. 2019:26:2282–2288.e3.

Gentet LJ, Avermann M, Matyas F, Staiger JF, Petersen CCH. Membrane potential dynamics of GABAergic neurons in the barrel cortex of behaving mice. *Neuron*. 2010:65:422–435.

Haegens S, Cousijn H, Wallis G, Harrison PJ, Nobre AC. Inter- and intra-individual variability in alpha peak frequency. *NeuroImage*. 2014:92:46–55.

Harris KD, Thiele A. Cortical state and attention. *Nat Rev Neurosci*. 2011:12:509–523.

Harris JA, Mihalas S, Hirokawa KE, Whitesell JD, Choi H, Bernard A, Bohn P, Caldejon S, Casal L, Cho A, et al. Hierarchical organization of cortical and thalamic connectivity. *Nature*. 2019:575:195–202.

Hasenstaub A, Shu Y, Haider B, Kraushaar U, Duque A, McCormick DA. Inhibitory postsynaptic potentials carry synchronized frequency information in active cortical networks. *Neuron*. 2005:47:423–435.

Herrero JL, Roberts MJ, Delicato LS, Gieselmann MA, Dayan P, Thiele A. Acetylcholine contributes through muscarinic receptors to attentional modulation in V1. *Nature*. 2008:454:1110–1114.

Innocenti GM, Manger PR, Masiello I, Colin I, Tettoni L. Architecture and callosal connections of visual areas 17, 18, 19 and 21 in the ferret (Mustela putorius). *Cereb Cortex*. 2002:12:411–422.

Isaacson JS, Scanziani M. How inhibition shapes cortical activity. *Neuron*. 2011:72:231–243.

Jacobs EAK, Steinmetz NA, Peters AJ, Carandini M, Harris KD. Cortical state fluctuations during sensory decision making. *Curr Biol*. 2020:30:4944–4955.e7.

Jarvis M, Mitra P. Sampling properties of the spectrum and coherency of sequences of action potentials. *Neural Comput*. 2001:13:717–749.

Johnson PCD, Barry SJE, Ferguson HM, Müller P. Power analysis for generalized linear mixed models in ecology and evolution. *Methods Ecol Evol*. 2015:6:133–142.

Joshi S. Pupillometry: arousal state or state of mind? *Curr Biol*. 2021:31:R32–R34.

Joshi S, Gold JI. Pupil size as a window on neural substrates of cognition. *Trends Cogn Sci*. 2020:24:466–480.

Joshi S, Li Y, Kalwani RM, Gold JI. Relationships between pupil diameter and neuronal activity in the locus coeruleus, colliculi, and cingulate cortex. *Neuron*. 2016:89:221–234.

Kaschube M. Neural maps versus salt-and-pepper organization in visual cortex. *Curr Opin Neurobiol*. 2014:24:95–102.

Kaschube M, Schnabel M, Löwel S, Coppola DM, White LE, Wolf F. Universality in the evolution of orientation columns in the visual cortex. *Science*. 2010:330:1113–1116.

Kass RE, Ventura V. Spike count correlation increases with length of time interval in the presence of trial-to-trial variation. *Neural Comput*. 2006:18:2583–2591.

Keller GB, Bonhoeffer T, Hübener M. Sensorimotor mismatch signals in primary visual cortex of the behaving mouse. *Neuron*. 2012:74:809–815.

Lansink CS, Goltstein PM, Lankelma JV, Pennartz CMA. Fast-spiking interneurons of the rat ventral striatum: temporal coordination of activity with principal cells and responsiveness to reward. *Eur J Neurosci*. 2010:32:494–508.

Lee K, Horien C, O'Connor D, Garand-Sheridan B, Tokoglu F, Scheinost D, Lake EMR, Constable RT. Arousal impacts distributed hubs modulating the integration of brain functional connectivity. *NeuroImage*. 2022:258:119364.

Lopes da Silva FH, Leeuwen WSV. The cortical source of the alpha rhythm. *Neurosci Lett*. 1977:6:237–241.

Leinweber M, Ward DR, Sobczak JM, Attinger A, Keller GB. A sensorimotor circuit in mouse cortex for visual flow predictions. *Neuron*. 2017:95:1420–1432.e5.

Lindeman S, Hong S, Kros L, Mejias JF, Romano V, Oostenveld R, Negrello M, Bosman LWJ, Zeeuw CID. Cerebellar Purkinje cells can differentially modulate coherence between sensory and motor cortex depending on region and behavior. *Proc Natl Acad Sci USA*. 2021:118:e2015292118.

Lopes da Silva FH, Vos JE, Mooibroek J, Rotterdam AV. Relative contributions of intracortical and thalamo-cortical processes in the generation of alpha rhythms, revealed by partial coherence analysis. *Electroen Clin Neuro*. 1980:50:449–456.

Mäki-Marttunen V. Pupil-based states of brain integration across cognitive states. *Neuroscience*. 2021:471:61–71.

Malkki HAI, Mertens PEC, Lankelma JV, Vinck M, van Schalkwijk FJ, van Mourik-Donga LB, Battaglia FP, Mahlke C, Kuhl D, Pennartz CMA. Effects of arc/Arg3.1 gene deletion on rhythmic synchronization of hippocampal CA1 neurons during locomotor activity and sleep. *Neurobiol Learn Mem*. 2016:131:155–165.

Manger PR, Nakamura H, Valentiniene S, Innocenti GM. Visual areas in the lateral temporal cortex of the ferret (*Mustela putorius*). *Cereb Cortex*. 2004:14:676–689.

Maris E, Oostenveld R. Nonparametric statistical testing of EEG- and MEG-data. *J Neurosci Methods*. 2007:164:177–190.

Maris E, Schoffelen J-M, Fries P. Nonparametric statistical testing of coherence differences. *J Neurosci Methods*. 2007:163:161–175.

Markov NT, Ercsey-Ravasz M, Essen DCV, Knoblauch K, Toroczkai Z, Kennedy H. Cortical high-density counterstream architectures. *Science*. 2013:342:1238406–1238406.

Markov NT, Vezoli J, Chameau P, Falchier A, Quilodran R, Huissoud C, Lamy C, Misery P, Giroud P, Ullman S, et al. Anatomy of hierarchy: feedforward and feedback pathways in macaque visual cortex. *J Comp Neurol*. 2014:522:225–259.

McCormick DA, McGinley MJ, Salkoff DB. Brain state dependent activity in the cortex and thalamus. *Curr Opin Neurobiol*. 2014:31C:133–140.

McGinley MJ, David SV, McCormick DA. Cortical membrane potential signature of optimal states for sensory signal detection. *Neuron*. 2015:87:179–192.

McGinley MJ, Vinck M, Reimer J, Batista-Brito R, Zagha E, Cadwell CR, Tolias AS, Cardin JA, McCormick DA. Waking state: rapid variations modulate neural and behavioral responses. *Neuron*. 2015:87:1143–1161.

Meijer GT, Montijn JS, Pennartz CMA, Lansink CS. Audiovisual modulation in mouse primary visual cortex depends on cross-modal stimulus configuration and congruency. *J Neurosci*. 2017:37:8783–8796.

Meijer GT, Marchesi P, Mejias JF, Montijn JS, Lansink CS, Pennartz CMA. Neural correlates of multisensory detection behavior: comparison of primary and higher-order visual cortex. *Cell Rep*. 2020:31:1–12, 107636.

Mejías JF, Wang X-J. Mechanisms of distributed working memory in a large-scale network of macaque neocortex. *Elife*. 2022:11:1–33, e72136.

Mejias JF, Murray JD, Kennedy H, Wang X-J. Feedforward and feedback frequency-dependent interactions in a large-scale laminar network of the primate cortex. *Sci Adv*. 2016:2: e1601335–e1601335.

Mitchell JF, Sundberg KA, Reynolds JH. Differential attention-dependent response modulation across cell classes in macaque visual area V4. *Neuron*. 2007:55:131–141.

Mitchell JF, Sundberg KA, Reynolds JH. Spatial attention decorrelates intrinsic activity fluctuations in Macaque area V4. *Neuron*. 2009:63:879–888.

Montijn JS, Goltstein PM, Pennartz CMA. Mouse V1 population correlates of visual detection rely on heterogeneity within neuronal response patterns. *Elife*. 2015:4:1–31, e10163.

Montijn JS, Meijer GT, Lansink CS, Pennartz CMA. Population-level neural codes are robust to single-neuron variability from a multidimensional coding perspective. *Cell Rep*. 2016:16:2486–2498.

Nandy AS, Nassi JJ, Reynolds JH. Laminar organization of attentional modulation in Macaque visual area V4. *Neuron*. 2017:93: 235–246.

Neske GT, Nestvogel D, Steffan PJ, McCormick DA. Distinct waking states for strong evoked responses in primary visual cortex and optimal visual detection performance. *J Neurosci*. 2019:39: 1226–1218.

Niell CM, Stryker MP. Modulation of visual responses by behavioral state in mouse visual cortex. *Neuron*. 2010:65:472–479.

Olcese U, Bos JJ, Vinck M, Lankelma JV, van Mourik-Donga LB, Schlumm F, Pennartz CMA. Spike-based functional connectivity in cerebral cortex and hippocampus: loss of global connectivity is coupled to preservation of local connectivity during non-REM sleep. *J Neurosci*. 2016:36:7676–7692.

Olcese U, Bos JJ, Vinck M, Pennartz CMA. Functional determinants of enhanced and depressed interareal information flow in nonrapid eye movement sleep between neuronal ensembles in rat cortex and hippocampus. *Sleep*. 2018:41:1969.

Oostenveld R, Fries P, Maris E, Schoffelen J-M. FieldTrip: open source software for advanced analysis of MEG, EEG, and invasive electrophysiological data. *Comput Intell Neurosci*. 2011:2011:156869.

Pachitariu M, Lyamzin DR, Sahani M, Lesica NA. State-dependent population coding in primary auditory cortex. *J Neurosci*. 2015:35:2058–2073.

Pachitariu M, Steinmetz N, Kadir S, Carandini M, Harris KD. Kilosort: realtime spike-sorting for extracellular electrophysiology with hundreds of channels. bioRxiv. 2016:061481. https://www.biorxiv.org/content/10.1101/061481v1

Pennartz CMA, Dora S, Muckli L, Lorteije JAM. Towards a unified view on pathways and functions of neural recurrent processing. *Trends Neurosci*. 2019:42:589–603.

Pesaran B, Vinck M, Einevoll GT, Sirota A, Fries P, Siegel M, Truccolo W, Schroeder CE, Srinivasan R. Investigating large-scale brain dynamics using field potential recordings: analysis and interpretation. *Nat Neurosci*. 2018:21:903–919.

Polack P-O, Friedman J, Golshani P. Cellular mechanisms of brain state-dependent gain modulation in visual cortex. *Nat Neurosci*. 2013:16:1331–1339.

Poulet JFA, Crochet S. The cortical states of wakefulness. *Front Syst Neurosci*. 2019:12:64.

Poulet JFA, Petersen CCH. Internal brain state regulates membrane potential synchrony in barrel cortex of behaving mice. *Nature*. 2008:454:881–885.

Reimer J, Froudarakis E, Cadwell CR, Yatsenko D, Denfield GH, Tolias AS. Pupil fluctuations track fast switching of cortical states during quiet wakefulness. *Neuron*. 2014:84:355–362.

Reimer J, McGinley MJ, Liu Y, Rodenkirch C, Wang Q, McCormick DA, Tolias AS. Pupil fluctuations track rapid changes in adrenergic and cholinergic activity in cortex. *Nat Commun*. 2016:7:13289.

Renart A, Machens CK. Variability in neural activity and behavior. *Curr Opin Neurobiol*. 2014:25:211–220.

Renart A, Rocha JDL, Bartho P, Hollender L, Parga N, Reyes A, Harris KD. The asynchronous state in cortical circuits. *Science*. 2010:327(5965):587–590.

Reynolds JH, Pasternak T, Desimone R. Attention increases sensitivity of V4 neurons. *Neuron*. 2000:26:703–714.

Ruff DA, Cohen MR. Attention can either increase or decrease spike count correlations in visual cortex. *Nat Neurosci*. 2014:17: 1591–1597.

Saalmann YB, Pinsk MA, Wang L, Li X, Kastner S. The pulvinar regulates information transmission between cortical areas based on attention demands. *Science*. 2012:337:753–756.

Saleem AB, Lien AD, Krumin M, Haider B, Roson MR, Ayaz A, Reinhold K, Busse L, Carandini M, Harris KD. Subcortical source and modulation of the narrowband gamma oscillation in mouse visual cortex. *Neuron*. 2017:93:315–322.

Sanchez-Vives MV, Massimini M, Mattia M. Shaping the default activity pattern of the cortical network. *Neuron*. 2017:94:993–1001.

Scheeringa R, Fries P, Petersson K-M, Oostenveld R, Grothe I, Norris DG, Hagoort P, Bastiaansen MCM. Neuronal dynamics underlying high- and low-frequency EEG oscillations contribute independently to the human BOLD signal. *Neuron*. 2011:69:572–583.

Schmitt LI, Wimmer RD, Nakajima M, Happ M, Mofakham S, Halassa MM. Thalamic amplification of cortical connectivity sustains attentional control. *Nature*. 2017:545:219–223.

Schneider DM, Nelson A, Mooney R. A synaptic and circuit basis for corollary discharge in the auditory cortex. *Nature*. 2014:513: 189–194.

Schneider M, Broggini AC, Dann B, Tzanou A, Uran C, Sheshadri S, Scherberger H, Vinck M. A mechanism for inter-areal coherence through communication based on connectivity and oscillatory power. *Neuron*. 2021:109:4050–4067.e12.

Schölvinck ML, Saleem AB, Benucci A, Harris KD, Carandini M. Cortical state determines global variability and correlations in visual cortex. *J Neurosci*. 2015:35:170–178.

Shadlen MN, Newsome WT. The variable discharge of cortical neurons: implications for connectivity, computation, and information coding. *J Neurosci*. 1998:18:3870–3896.

Siegle JH, Pritchett DL, Moore CI. Gamma-range synchronization of fast-spiking interneurons can enhance detection of tactile stimuli. *Nat Neurosci*. 2014:17:1371–1379.

Singer W. Neuronal oscillations: unavoidable and useful? *Eur J Neurosci*. 2018:48:2389–2398.

Snyder AC, Morais MJ, Kohn A, Smith MA. Correlations in V1 are reduced by stimulation outside the receptive field. *J Neurosci*. 2014:34:11222–11227.

Sohal VS, Zhang F, Yizhar O, Deisseroth K. Parvalbumin neurons and gamma rhythms enhance cortical circuit performance. *Nature*. 2009:459:698–702.

Spyropoulos G, Saponati M, Dowdall JR, Schölvinck ML, Bosman CA, Lima B, Peter A, Onorato I, Klon-Lipok J, Roese R, et al. Spontaneous variability in gamma dynamics described by a damped harmonic oscillator driven by noise. *Nat Commun*. 2022:13:2019.

Steriade M. Grouping of brain rhythms in corticothalamic systems. *Neuroscience*. 2006:137:1087–1106.

Steriade M, McCormick DA, Sejnowski TJ. Thalamocortical oscillations in the sleeping and aroused brain. *Science*. 1993:262:679–685.

Steriade M, Timofeev I, Grenier F. Natural waking and sleep states: a view from inside neocortical neurons. *J Neurophysiol*. 2001:85:1969–1985.

Stitt I, Zhou ZC, Radtke-Schuller S, Fröhlich F. Arousal dependent modulation of thalamo-cortical functional interaction. *Nat Commun*. 2018:9:2455.

Tuerlinckx F, Rijmen F, Verbeke G, Boeck P. Statistical inference in generalized linear mixed models: a review. *Br J Math Statistical Psychol*. 2006:59:225–255.

van Kerkoerle T, Self MW, Dagnino B, Gariel-Mathis M-A, Poort J, van der Togt C, Roelfsema PR. Alpha and gamma oscillations characterize feedback and feedforward processing in monkey visual cortex. *Proc Natl Acad Sci U S A*. 2014:111:14332–14341.

Veit J, Hakim R, Jadi MP, Sejnowski TJ, Adesnik H. Cortical gamma band synchronization through somatostatin interneurons. *Nat Neurosci*. 2017:20:951–959.

Vinck M, Oostenveld R, van Wingerden M, Battaglia F, Pennartz CMA. An improved index of phase-synchronization for electrophysiological data in the presence of volume-conduction, noise and sample-size bias. *NeuroImage*. 2011:55:1548–1565.

Vinck M, Battaglia FP, Womelsdorf T, Pennartz CMA. Improved measures of phase-coupling between spikes and the local field potential. *J Comput Neurosci*. 2012:33:53–75.

Vinck M, Batista-Brito R, Knoblich U, Cardin JA. Arousal and locomotion make distinct contributions to cortical activity patterns and visual encoding. *Neuron*. 2015:86:740–754.

Vinck M, Bos JJ, Mourik-Donga LAV, Oplaat KT, Klein GA, Jackson JC, Gentet LJ, Pennartz CMA. Cell-type and state-dependent synchronization among rodent somatosensory, visual, perirhinal cortex, and hippocampus CA1. *Front Syst Neurosci*. 2016:9:111.

Vogels R, Spileers W, Orban GA. The response variability of striate cortical neurons in the behaving monkey. *Exp Brain Res*. 1989:77:432–436.

Vyazovskiy VV, Olcese U, Hanlon EC, Nir Y, Cirelli C, Tononi G. Local sleep in awake rats. *Nature*. 2011:472:443–447.

Wainstein G, Rojas-Líbano D, Medel V, Alnæs D, Kolskår KK, Endestad T, Laeng B, Ossandon T, Crossley N, Matar E, et al. The ascending arousal system promotes optimal performance through mesoscale network integration in a visuospatial attentional task. *Netw Neurosci*. 2021:5:890–910.

Wang C-A, Munoz DP. A circuit for pupil orienting responses: implications for cognitive modulation of pupil size. *Curr Opin Neurobiol*. 2015:33:134–140.

Wang C-A, Blohm G, Huang J, Boehnke SE, Munoz DP. Multisensory integration in orienting behavior: pupil size, microsaccades, and saccades. *Biol Psychol*. 2017:129:36–44.

Waschke L, Kloosterman NA, Obleser J, Garrett DD. Behavior needs neural variability. *Neuron*. 2021:109:751–766.

Wen H, Liu Z. Separating fractal and oscillatory components in the power spectrum of neurophysiological signal. *Brain Topogr*. 2015:29:13–26.

Wilson HR, Cowan JD. Excitatory and inhibitory interactions in localized populations of model neurons. *Biophys J*. 1972:12:1–24.

Zagha E, Casale AE, Sachdev RNS, McGinley MJ, McCormick DA. Motor cortex feedback influences sensory processing by modulating network state. *Neuron*. 2013:79:567–578.